energies

MDPI

Article

Two-Phase Flow Distribution in Plate Heat Exchangers Using a Coupled CFD–Distributed Parameter Model

Lin He [1,2], Zhipeng Ye [2], Shunan Zhao [2], Qing Luo [2], Bin Li [2] and Zhichun Liu [1,*]

[1] School of Energy and Power Engineering, Huazhong University of Science and Technology, Wuhan 430074, China; helin861217@outlook.com
[2] Gree Electric Appliances Inc. of Zhuhai, Zhuhai 519070, China; 18659671173@163.com (Z.Y.); zhaoshunan0216@163.com (S.Z.); jixingchadehen@163.com (Q.L.); 18800178849@163.com (B.L.)
* Correspondence: zcliu@hust.edu.cn

Abstract

Plate heat exchangers (PHEs) play a critical role in the energy efficiency of heat pump systems. However, non-uniform two-phase flow distribution across parallel channels remains a key limitation, as it may cause local dryout and degrade heat transfer performance. To address the limitations of existing prediction approaches, a hybrid modeling framework coupling computational fluid dynamics (CFD) simulations with a distributed parameter model is developed. The model is validated against experimental data under 12 representative operating conditions. The results show that the average prediction errors for the total mass flow rate, pressure drop, and heat transfer rate are within 3%, ±10%, and ±5%, respectively. The influences of refrigerant outlet conditions and inlet distributor geometry on flow distribution uniformity are systematically investigated, identifying the dominant factors governing pressure drop and the mechanism by which distributor orientation improves uniformity. Quantitative optimization shows that an orifice orientation of 225° reduces flow non-uniformity by 67.8% and enhances the heat transfer rate by 4.33% compared with the distributor-free design. The proposed method is robust across various operating scenarios and provides a reliable, quantitative tool for optimizing PHE inlet distributor designs.

Keywords: plate heat exchanger; two-phase flow distribution; CFD; distributed parameter model

1. Introduction

Heat pump technology has emerged as a key enabler of energy efficiency amid the global energy transition. In these systems, plate heat exchangers (PHEs) play a central role in efficient thermal energy transfer and their performance significantly affects the overall energy efficiency of the system [1]. However, flow maldistribution within PHEs remains a persistent challenge, stemming from inlet geometry, two-phase flow characteristics, operating condition fluctuations and other influential factors. Flow maldistribution significantly increases the risk of local dryout [2], thereby impairing heat transfer performance. This phenomenon not only constrains design optimization and operational performance but also constitutes a primary bottleneck hindering the realization of theoretical heat transfer efficiencies. Under the growing emphasis on energy conservation and emission

Academic Editor: Artur Blaszczuk

Received: 19 May 2026
Revised: 24 June 2026
Accepted: 3 July 2026
Published: 7 July 2026

reduction, accurate prediction of flow distribution holds significant research importance for optimizing PHE structural design and enhancing system energy efficiency.

Experimental approaches are commonly categorized into direct or indirect methods for studying the flow distribution characteristics of PHEs. Direct methods rely on physical phase separation using special devices to isolate vapor and liquid phases, followed by individual flow rate measurements via sensors [3–9]. Alternatively, the two-phase refrigerant was superheated to achieve complete vaporization, followed by flow rate measurement using a gas mass flow meter. The vapor quality and phase proportions were determined using mass and energy conservation laws [10–14]. While direct methods can achieve high-precision flow measurements, they require complex experimental setups and involve cumbersome procedures. Moreover, the addition of phase separation devices and sensors inevitably disturbed the original flow field, altering the actual flow distribution within PHEs. Given that PHE channel dimensions are in the millimeter range, synchronous flow measurements across all parallel channels were hindered by the physical size of a conventional sensor. To better capture the true flow characteristics within the heat exchanger, researchers have developed indirect measurement methods based on distributed parameter models. These methods integrated performance testing with infrared thermography to reconstruct two-phase flow distribution, enabling channel-level predictions. Li et al. [15] quantitatively analyzed two-phase refrigerant flow distribution using infrared images. A mapping between the heat transfer capacities of the two fluid streams was established, then flow distribution could be determined through an iterative algorithm. Li et al. [16] developed a one-dimensional finite volume model to calculate the surface temperature distribution and combined it with the length of the subcooled region from infrared images to predict the liquid flow distribution. Navarro et al. [17,18] used infrared thermography to capture thermal images of the water-side end face of a PHE with a distributor. They systematically analyzed the effects of inlet dryness, outlet superheated temperature, and water temperature difference on flow non-uniformity, and proposed the SEWTLE algorithm (Semi-Explicit method for Wall-Temperature-Linked Equations) for efficient flow prediction. Li et al. [19,20] measured the wall temperature of the heat exchanger using an infrared camera. The triangular threshold method to determine the phase transition boundary line was employed, and a two-phase distributed parameter model was established. Taking the pressure drop and the phase transition boundary line as constraint conditions, they quantified the flow distribution in each channel. Zhang et al. [21] constructed a simplified evaporator model for the two-phase and superheated regions of a PHE, calibrated it using infrared camera as optimization targets, and conducted qualitative analysis of refrigerant distribution under different inlet configurations. Li et al. [22] established an experimental platform for infrared monitoring of PHEs and obtained thermal images of the evaporator side and end face under steady-state conditions. A three-dimensional phase boundary model and a thermal image processing method tailored for corrugated surfaces were proposed, enabling a complete framework for flow distribution reconstruction. The indirect methods offered non-invasive monitoring with minimal flow field disturbance, making them suitable for complex operating conditions.

Indirect methods for measuring flow distribution in PHEs usually depend on distributed parameter models. The accuracy of these models is highly sensitive to the choice of empirical correlations and the validity of underlying assumptions. However, most empirical correlations are applicable only within limited ranges. For pressure drop in the inlet header, most studies adopt T-junction empirical models [23–25], which perform well for standard PHEs. However, flow in the header is highly non-uniform in PHEs with complex distributors, and traditional T-junction models fail to predict local flow characteristics. The application of these correlations will introduce significant pressure drop errors, de-

grading flow distribution prediction accuracy. Additionally, indirect methods often employ the phase transition interface from an infrared camera as a model constraint. However, under low outlet superheated temperature conditions, some channels may lack a clear superheated region, making the interface difficult to identify [26]. Consequently, accurate identification and quantification of these interfaces become challenging. This limitation severely compromises the reliability and accuracy of indirect measurement techniques under such operating conditions.

Given the inherent limitations of experimental studies, computational fluid dynamics (CFD) has become a widely adopted approach for predicting two-phase flow distribution in PHEs. However, the flow channels in PHEs are based on complex corrugated plates, and full-scale modeling requires substantial computational resources and sophisticated meshing strategies [27,28]. Moreover, two-phase flow processes are influenced by multiple interacting factors, and inappropriate parameter settings can lead to non-physical results. Therefore, developing high-fidelity CFD models and appropriately specifying simulation parameters pose major challenges. Flavio et al. [29] developed and experimentally validated a CFD model of a rectangular-channel PHE, achieving good agreement between simulations and measurements, thereby demonstrating the feasibility of CFD for multi-channel parallel structures. However, the use of an idealized rectangular channel, which was distinct from real corrugated geometries, limited its applicability to structural optimization studies. Pawar and Maurya [30] developed a simplified three-dimensional CFD model with rectangular channels to investigate the effects of Reynolds number and wall temperature on flow distribution uniformity in air-water flow. However, they neglected the role of corrugated structures in turbulence generation and flow resistance, resulting in discrepancies between simulations and actual flow state. Qiu et al. [31] simplified the model by omitting corrugation details and replacing them with flat plate channels. The simplification reduced computational cost but undermined the physical realism of flow resistance and turbulence, thereby compromising result reliability. Zhang et al. [32] constructed a simplified model of the inlet header with distributors, setting the outlet of all branches to zero-pressure boundary conditions, and obtained the influence of different distributor designs on flow distribution. However, this assumption ignored the pressure gradient differences among branches in actual flow, making it difficult to reflect the flow distribution mechanism accurately. Mudhafar [33] developed a full numerical model of chevron PHEs using the Volume of Fluid (VOF) method to compare two-phase flow distribution in PHEs with and without distributors. The effects of structural parameters and operating conditions were systematically analyzed. However, heat transfer effects were not included, and the mesh was relatively coarse, potentially affecting phase interface resolution. Ham et al. [34] proposed a method coupling the ε-NTU model with CFD simulations to address single-phase flow distribution in PHEs. This simplification enables feasible CFD simulations for full-scale PHEs, whereas fully resolving corrugated geometries would be prohibitively expensive. However, the highly simplified assumptions in the ε-NTU model limit its ability to capture nonlinear heat transfer during phase transition, thereby restricting its application range.

In light of the preceding literature, it can be concluded that existing methods for predicting two-phase flow distribution in PHEs are constrained by complex experimental setups, limited applicability, and substantial computational cost. To overcome these limitations, the present study proposes a hybrid method that integrates CFD simulation with a distributed parameter model correction.

In this method, a geometrically simplified CFD model is first developed by omitting the corrugation details of the plate channels to generate an initial prediction of vapor-liquid flow distribution. Subsequently, a distributed parameter model is applied to correct

these results, compensating for errors introduced by geometric simplification. The proposed method is validated against experimental data on a 54-plate chevron PHE under 12 operating conditions. Furthermore, the method is applied to predict flow distribution under various outlet conditions and distributor designs, and quantitative design rules for distributor optimization are derived. These results demonstrate that the proposed method exhibits broad applicability across diverse operating conditions and geometric configurations, facilitating the analysis of flow distribution and enabling structural optimization of PHEs.

2. Indirect Measurement of Flow Distribution

Flow distribution measurement methods are typically classified into two categories: direct and indirect. Direct methods involve the physical separation of vapor and liquid phases to quantify individual flow rates; however, these techniques are intrusive, significantly disturbing the flow field, and necessitate complex experimental setups. In contrast, an indirect measurement strategy is employed in this study, following the methodology proposed by Li and Hrnjak [20]. Rather than measuring flow rates directly, the flow distribution is inferred by coupling IR-captured wall temperature fields with a distributed-parameter model. This non-invasive approach minimizes flow disturbance while enabling the accurate determination of flow rates for each individual channel.

2.1. Experiment Description

Figure 1 illustrates the schematic diagram of the test system, consisting of two loops: a refrigerant (R32) loop and a water loop.

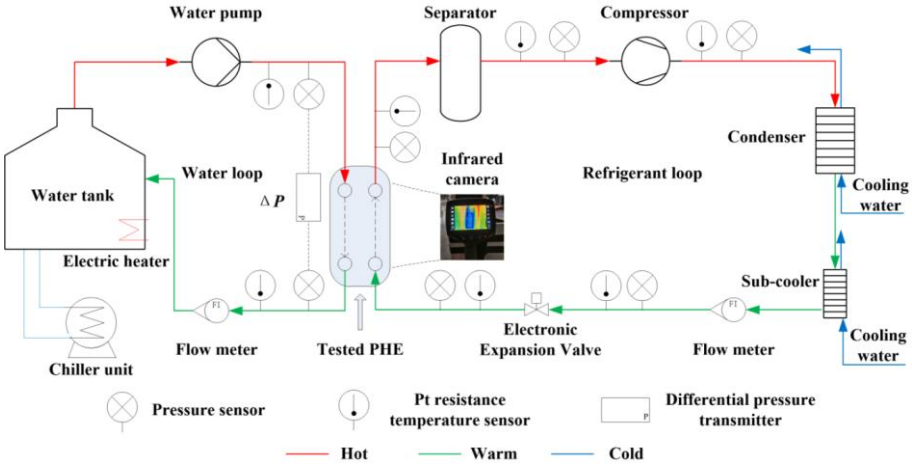

Figure 1. Experimental system of flow measurement.

In the refrigerant loop, the vapor R32 is compressed and subsequently directed to the condenser and sub-cooler. Following complete condensation into the sub-cooled liquid state, the mass flow rate of the refrigerant is measured using a flow meter. Subsequently, the R32 passes through an electronic expansion valve, undergoing throttling and emerging as a two-phase mixture. Then, the R32 enters the refrigerant side of the PHE through the lower inlet, exchanges heat with the water and exits through the upper outlet. After passing through a vapor-liquid separator, the R32 returns to the compressor, thereby completing the cycle.

The water loop supplies temperature-controlled water to the PHE. The water releases heat to the refrigerant in the PHE and then returns to the constant-temperature water tank. The tank temperature is maintained by a PID controller that dynamically adjusts both an electric heater and a chiller unit in response to the real-time temperature deviation. The

chiller cools the water when the tank temperature rises above the setpoint, while the electric heater activates when the temperature drops below the setpoint. The refrigerant outlet superheated temperature is regulated by adjusting the water flow rate using a variable-frequency pump.

Temperature and pressure sensors are installed upstream of the expansion valve and at both the inlet and outlet of the PHE. The outlet superheated temperature is precisely regulated by controlling the temperature and pressure upstream of the expansion valve. The enthalpy before the valve is calculated from the measured temperature and pressure, and assuming constant enthalpy during throttling, the enthalpy at the PHE inlet is determined. Together with the measured inlet pressure of the heat exchanger, this enthalpy is used to calculate the inlet vapor quality using REFPROP.

A 54-plate chevron-type PHE is selected for testing, and the geometric parameters of the plates are summarized in Table 1. An infrared (IR) camera is installed to capture the surface temperature distribution on the external sidewalls of the PHE. The resolution of the IR camera is 640 × 512 pixels, the temperature measurement accuracy is ±2 °C, the thermal sensitivity is 35 mK, and the temperature measurement range is from −20 °C to 650 °C. To minimize radiative interference from the surroundings, a highly reflective coating is applied to the surface of PHE, and an opaque shell is installed along the line of sight of the IR camera, as shown in Figure 2.

Table 1. Plate geometry of the PHE.

Geometric Parameter	Value
Chevron angle	65°
Corrugation depth	1.3 mm
Corrugation pitch	4.7 mm
Plate thickness	0.36 mm
Port length	286 mm
Total length	326 mm
Port width	75.3 mm
Total width	116 mm
Water inlet header diameter	35 mm
Water outlet header diameter	35 mm
Refrigerant inlet header diameter	25.3 mm
Refrigerant outlet header diameter	35 mm

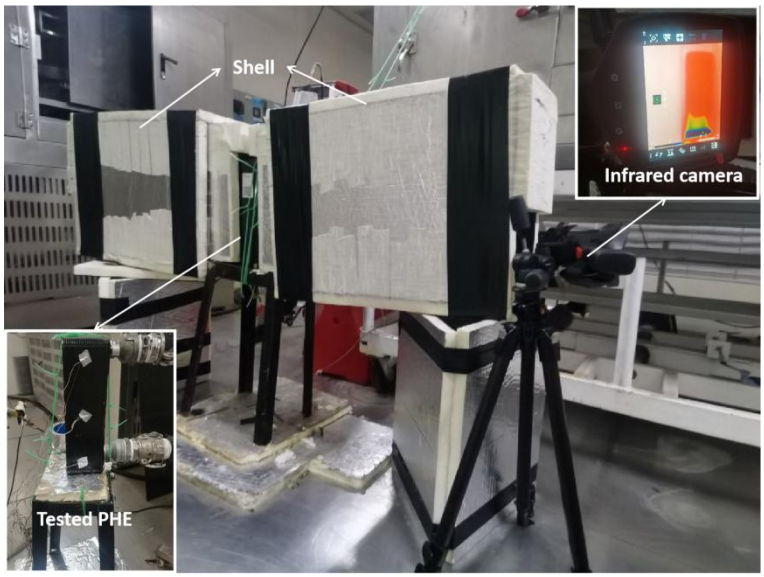

Figure 2. Infrared temperature measurement devices.

The entire test system is controlled by a programmable logic controller (PLC) through feedback regulation, ensuring stable operation of key parameters such as temperature, pressure, and flow rate. All instruments are calibrated and the measurement uncertainties are summarized in Table 2.

Table 2. Measurement accuracy.

Measured Parameter	Accuracy
Platinum resistance temperature	±0.2 °C
Infrared temperature	±2 °C
Refrigerant mass flow rate	±0.2%
Water mass flow rate	±0.2%
Absolute Pressure	±0.25%
Differential Pressure	±0.075%

2.2. Flow Distribution Measurement Method

2.2.1. Distributed Parameter Model

An indirect measurement method is employed to determine the flow distribution in the PHE, taking into account the coupled heat transfer between the water and refrigerant sides. Flow distribution models for both sides are developed independently, as shown in Figure 3. The PHE model is divided into three regions on each side, including the inlet header, plate channels, and outlet header. Each region is discretized into independent elements and are defined for each side to enable coupled thermal modeling. For a PHE with $(2N + 2)$ plates, where N denotes the number of refrigerant channels, there are N refrigerant-side and $(N + 1)$ water-side channels. Heat transfer in the headers is neglected, and thermal coupling between the water and refrigerant occurs exclusively within the plate channels.

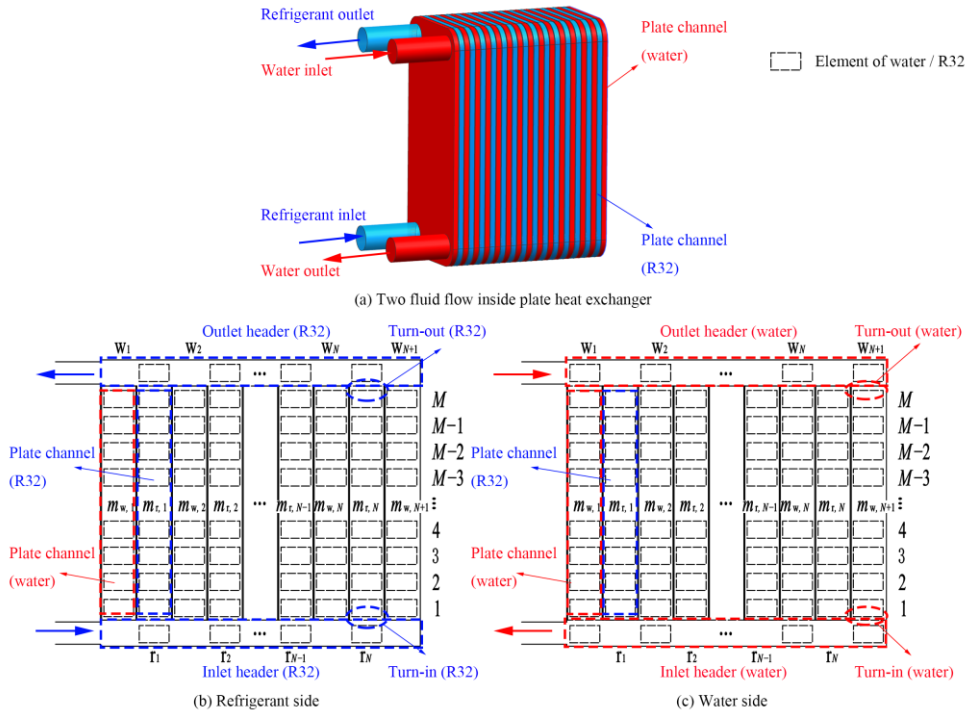

Figure 3. Distributed parameter model.

For the water side and refrigerant side, the pressure drop in each branch channel can be calculated by Equation (1):

$$\Delta P_i = \sum_{k=1}^{i} \Delta P_{\mathrm{ih},k} + \Delta P_{\mathrm{turn-in},i} + \Delta P_{\mathrm{ch},i} + \Delta P_{\mathrm{turn-out},i} + \sum_{k=1}^{i} \Delta P_{\mathrm{oh},k} \quad (1)$$

In the formula, ΔP_i is the total pressure drop in the branch channel, $\sum \Delta P_{\mathrm{ih,k}}$ is the inlet header pressure drop, $\Delta P_{\mathrm{turn\text{-}in},i}$ is the turning-in pressure drop, $\Delta P_{\mathrm{ch},i}$ is the plate channel pressure drop, $\Delta P_{\mathrm{turn\text{-}out},i}$ is the outlet turning pressure drop, and $\sum \Delta P_{\mathrm{oh},k}$ is the outlet header pressure drop.

For the water side, after the total pressure drop in each branch channel is calculated, the flow rates are adjusted according to the principle of equal pressure drop, enabling iterative determination of the water flow distribution [35]. For the refrigerant side, the number of unknowns increases, making it impossible to determine a unique solution for the two-phase flow distribution based on pressure drop balance conditions alone. Therefore, an additional constraint, the location of the phase boundary between the two-phase and superheated zones, is introduced to enable a simultaneous solution of the vapor and liquid flow distribution. The location of the phase transition boundary is determined using an IR camera together with image processing algorithms that analyze the IR temperature images to extract the phase change interface.

The heat transfer in each element between water and refrigerant in the plate channel can be calculated by Equation (2).

$$Q_{(i,j)} = \left(U_{(i,j),\mathrm{left}} \Delta T_{\mathrm{m},(i,j),\mathrm{left}} + U_{(i,j),\mathrm{right}} \Delta T_{\mathrm{m},(i,j),\mathrm{right}}\right) A_{\mathrm{eff}} \quad (2)$$

In the formula, $Q_{(i,j)}$ represents the heat transfer rate of the (i, j) element in the plate channel, A_{eff} represents the effective heat transfer area on one side of each plate, $U_{(i,j),\mathrm{left}}$ and $U_{(i,j),\mathrm{right}}$ represent the overall heat transfer coefficients at the left and right boundaries of the (i, j) element in the plate channel, and $\Delta T_{\mathrm{m},(i,j),\mathrm{left}}$ and $\Delta T_{\mathrm{m},(i,j),right}$ represent the logarithmic mean temperature differences at the left and right boundaries of the (i, j) element in the plate channel, respectively.

The pressure drops and heat transfer rates for each region defined in Equations (1) and (2) are calculated using empirical correlations, the sources of which are provided in Table 3. Based on the conservation equations of mass, momentum, and energy, combined with the empirical correlations, the pressure drops and heat transfer rates of each differential element on the water side and refrigerant side can be solved. The two-phase refrigerant flow distribution is then obtained through an iterative numerical procedure. The underlying principle and numerical implementation of this method are described in Reference [15].

Before applying the model to predict flow distribution, the empirical correlations in the distributed parameter model were calibrated against experimental data obtained from the same 54-plate PHE. This calibration enables the distributed parameter model to accurately reproduce the baseline thermal-hydraulic performance. Since the calibration coefficients are specific to the current plate geometry and operating conditions, they are not presented as universal values. If this modeling framework is applied to different refrigerants or plate geometries, recalibration against experimental data is necessary.

Table 3. Summary of selected correlations.

Items	Correlations
Water side (in-channel)	
Heat transfer coefficient	Li and Hrnjak [36]
Refrigerant side (in-channel)	
Single-phase heat transfer coefficient	Li and Hrnjak [36]
Single-phase frictional pressure drop	Li and Hrnjak [35]
Two-phase heat transfer coefficient	Almalfi et al. [37]
Two-phase frictional pressure drop	Almalfi et al. [37]
Gravitational pressure drop	Homogeneous model

Acceleration pressure drop	Homogeneous model
Local turning-in pressure loss	Buell et al. [23]
Local turning-out pressure loss	Collier and Thome [38]
Refrigerant side (outlet header)	
Frictional pressure drop	Homogeneous model + Blasius correlation
Acceleration pressure drop	Homogeneous model

2.2.2. Calculation Process of Mass Flow Rate

The overall workflow of the indirect flow distribution measurement method is illustrated in Figure 4. First, thermal-hydraulic performance tests of the PHE are conducted. Using the measured inlet water flow rate, the water-side flow distribution is determined based on the principle of equal pressure drop across parallel channels. Meanwhile, initialization for the vapor and liquid flow rates in each channel are set based on the total refrigerant inlet flow rate and temperature. Using these initial values, the distributed parameter model is employed to compute the pressure drop and heat transfer in each element on both the water and refrigerant sides. The vapor flow rates are iteratively adjusted to equalize the pressure drops across all parallel channels. The updated vapor flow rate is then input into the model for re-calculation. This iteration continues until the pressure drops converge across all channels, yielding the vapor flow distribution. Using the preliminary liquid flow distribution, the quality in each element is calculated to determine the phase transition boundary between the two-phase and superheated zones. Subsequently, infrared camera is used to measure the temperature distribution on the external plate of the PHE. An image processing algorithm is used to extract the phase transition boundary location, which serves as a reference for comparison with the predicted boundary from the distributed parameter model. The liquid flow rate is adjusted based on the deviation between the predicted and measured phase transition boundaries. The updated value is then input into the model for re-calculation. This iteration continues until the predicted phase boundary converges to the experimental one, yielding the final liquid flow distribution.

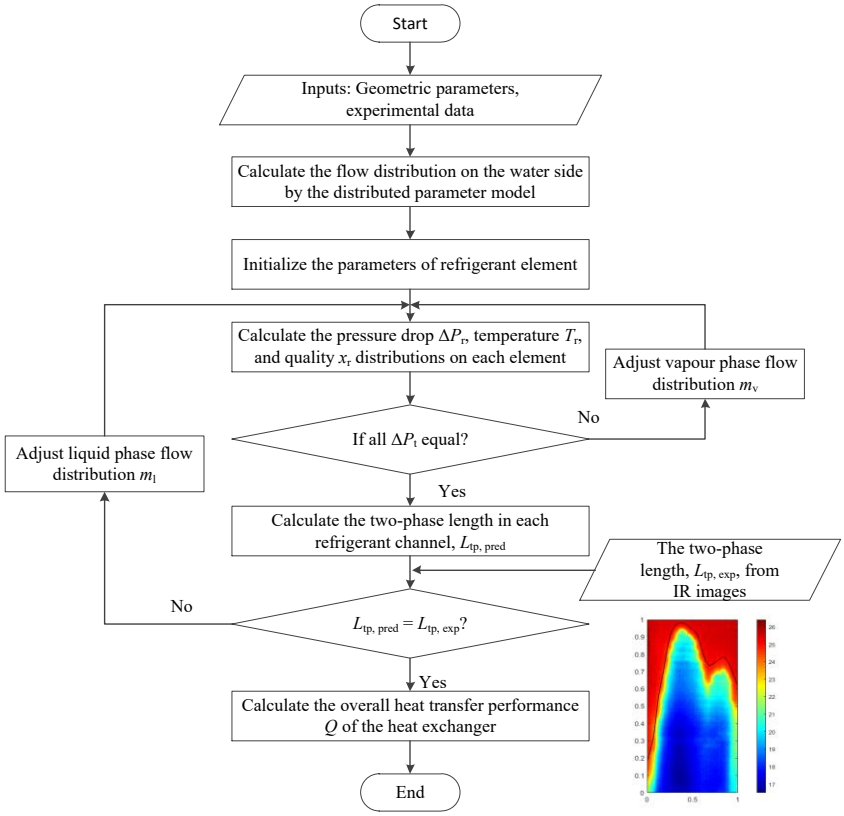

Figure 4. Mass flow rate calculation process of indirect measurement method.

3. Coupled Model for Flow Distribution Prediction

The indirect flow distribution measurement method is non-intrusive and allows simultaneous measurement of flow in multiple channels. However, this method relies on empirical correlations, requiring experimental calibration of model parameters for each geometry to ensure prediction accuracy, thereby limiting its applicability to the optimization of inlet header designs. To address these limitations, we employ a hybrid method coupling CFD with a distributed parameter model. By eliminating empirical correlations for inlet header pressure drops, this approach avoids geometry-specific recalibration and renders the optimization of various distributor configurations computationally feasible.

3.1. Geometry

As shown in Figure 5, the flow passages formed by stacking the corrugated PHE plates exhibit complex three-dimensional geometries. Constructing a full-scale model can result in geometry files exceeding tens or even hundreds of gigabytes (GB). Moreover, the two-phase flow and heat transfer process exhibits a highly nonlinear relationship, making it computationally prohibitive for conventional platforms to perform two-phase conjugate heat transfer simulations in a full PHE model.

To reduce computational cost and focus on key flow regions, the full PHE geometry is simplified in this study. As shown in Figure 6a, the computational domain is limited to a local region extending 90 mm from the bottom of the PHE. The corrugated surface structure is neglected, the plate channels are modeled as rectangular ducts, and heat transfer within the channels is not resolved. Since the inlet header geometry is preserved and heat transfer within inlet header is not resolved, this simplification introduces negligible error in the flow characteristics within the inlet header, while primarily affecting pressure drop and heat transfer predictions in other regions (particularly the plate channels).

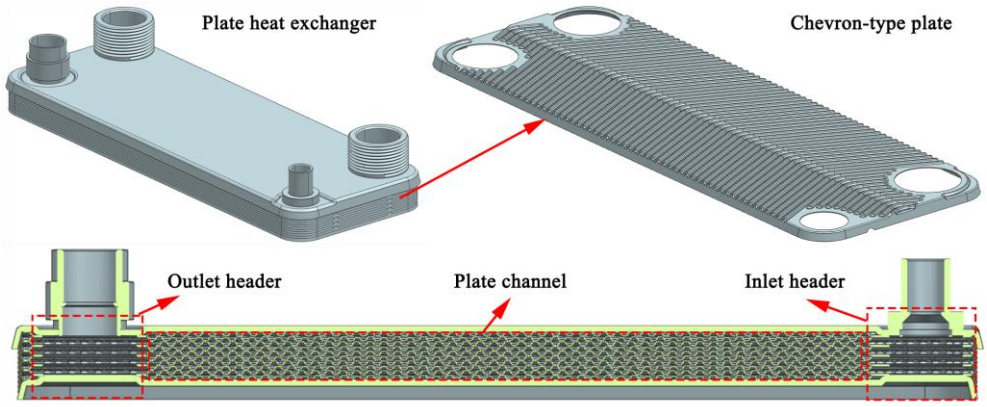

Figure 5. Chevron-type plate and PHE model.

For PHEs without distributors, the corrugated structure causes a significantly higher pressure drop in the plate channels $\Delta P_{ch,i}$ than in the inlet/outlet header, leading to nearly uniform outlet pressures across all branch channels. However, in this study, the plate channels are modeled as smooth rectangular ducts, neglecting the flow resistance and turbulence enhancement from the corrugated structure, resulting in a underestimation of $\Delta P_{ch,i}$. If only one outlet boundary is applied, the total pressure drop ΔP_i would be overly sensitive to inlet header flow characteristics, hindering accurate prediction of the actual pressure gradient distribution. To improve simulation accuracy, independent outlet boundary conditions are applied to all 26 branch channels.

Owing to the reduced flow resistance from model simplification, non-physical backflow may occur near the outlet boundaries. The backflow may trigger non-physical oscillations in the velocity and phase fields, thereby compromising numerical convergence. To suppress these instabilities, a 30-mm-long straight extension is added at the exit of each branch channel. Numerical results show that this outlet extension significantly improves computational stability and effectively suppresses backflow with mesh independence and convergence ensured.

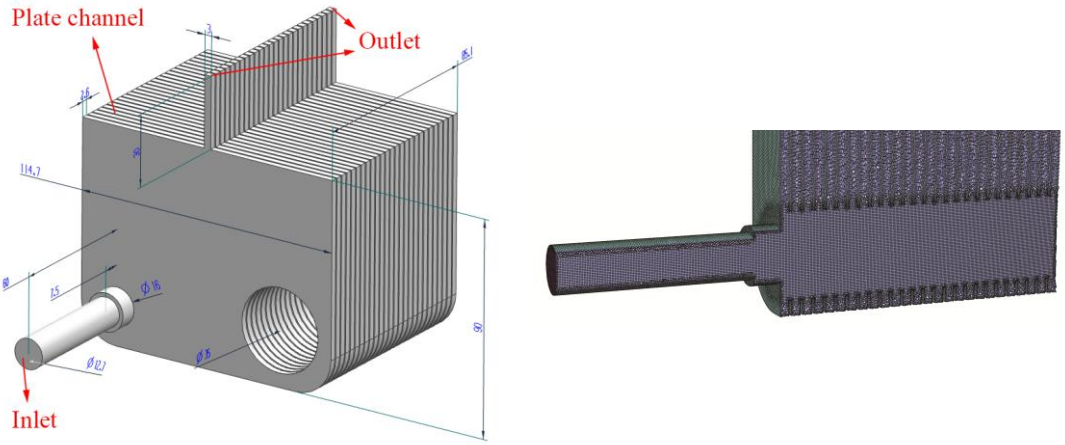

(**a**) (**b**)

Figure 6. (**a**) Fluid domain and (**b**) mesh.

3.2. Mathematical Model

To ensure computational feasibility, the following modeling assumptions are adopted, guided by physical insight and engineering constraints:

(1) The fluid in PHE is treated as continuous, incompressible, Newtonian fluids.
(2) The compressor oil entrained in the system is neglected, and only the vapor and liquid phases of the refrigerant are considered.
(3) The vapor phase is treated as the primary phase and the liquid phase as the secondary phase, with the droplet diameter held constant; coalescence and breakup of the dispersed phase are neglected.
(4) Heat transfer is neglected, while mass and momentum transfer are resolved.

The constant-diameter assumption is justified as follows: in the inlet header, flow distribution is governed primarily by pressure gradient and inertia, rather than by turbulent eddy–droplet interactions; the droplet residence time is also short, making breakup and coalescence secondary. This simplification is standard in Eulerian–Eulerian header flow simulations. Panda et al. [39] used fixed Interaction Length Scale (ILS) values to prescribe the effective mean diameter of dispersed droplets in their Hybrid Eulerian Multiphase model of refrigerant distribution in headers, and their sensitivity analysis confirmed that ILS variations have a limited effect on the macroscopic distribution. Additionally, systematic error introduced by this simplification is compensated by the distributed-parameter model correction (Section 3.5), whose empirical correlations implicitly account for the macroscopic effects of droplet size evolution.

The two-phase flow of R32 is simulated using the following governing equations:

3.2.1. Conservation Equations

Mass conservation [40]:

$$\frac{\partial}{\partial t}(\alpha_l \rho_l) + \nabla \cdot (\alpha_l \rho_l \vec{v}_l) = \sum_{p=1}^{n} (\dot{m}_{vl} - \dot{m}_{lv}) \tag{3}$$

$$\frac{\partial}{\partial t}(\alpha_v \rho_v) + \nabla \cdot (\alpha_v \rho_v \vec{v}_v) = \sum_{p=1}^{n} (\dot{m}_{lv} - \dot{m}_{vl}) \tag{4}$$

where, $\vec{v}_l$, $\vec{v}_v$ represent the velocities of liquid and vapor phase, $\dot{m}_{lv}$ is mass transfer from liquid phase to vapor phase, $\dot{m}_{vl}$ is mass transfer from vapor phase to liquid phase.

Momentum conservation [40]:

$$\begin{aligned} \frac{\partial}{\partial t}(\alpha_l \rho_l \vec{v}_l) + \nabla \cdot (\alpha_l \rho_l \vec{v}_l \vec{v}_l) &= -\alpha_l \nabla P + \nabla \cdot \bar{\bar{\tau}}_l + \alpha_l \rho_l \vec{g} \\ &+ \left(\vec{R}_{vl} + \dot{m}_{vl} \vec{v}_{vl} - \dot{m}_{lv} \vec{v}_{lv}\right) \\ &+ \left(\vec{F}_l + \vec{F}_{lift,l} + \vec{F}_{wl,l} + \vec{F}_{vm,l} + \vec{F}_{td,l}\right) \end{aligned} \tag{5}$$

$$\begin{aligned} \frac{\partial}{\partial t}(\alpha_v \rho_v \vec{v}_v) + \nabla \cdot (\alpha_v \rho_v \vec{v}_v \vec{v}_v) &= -\alpha_v \nabla P + \nabla \cdot \bar{\bar{\tau}}_v + \alpha_v \rho_v \vec{g} \\ &+ \left(\vec{R}_{lv} + \dot{m}_{lv} \vec{v}_{lv} - \dot{m}_{vl} \vec{v}_{vl}\right) \\ &+ \left(\vec{F}_v + \vec{F}_{lift,v} + \vec{F}_{wl,v} + \vec{F}_{vm,v} + \vec{F}_{td,v}\right) \end{aligned} \tag{6}$$

$$\bar{\bar{\tau}}_l = \alpha_l \mu_l \left(\nabla \vec{v}_l + \nabla \vec{v}_l^{T}\right) + \alpha_l \left(\lambda_l - \frac{2}{3}\mu_l\right) \nabla \cdot \vec{v}_l \bar{\bar{I}} \tag{7}$$

$$\bar{\bar{\tau}}_v = \alpha_v \mu_v \left(\nabla \vec{v}_v + \nabla \vec{v}_v^{T}\right) + \alpha_v \left(\lambda_v - \frac{2}{3}\mu_v\right) \nabla \cdot \vec{v}_v \bar{\bar{I}} \tag{8}$$

$$\vec{R}_{lv} = -\vec{R}_{vl} = K_{lv}(\vec{v}_l - \vec{v}_v) \tag{9}$$

Here, μ_l and μ_v are the shear viscosity of the liquid and vapor phases, respectively; λ_l and λ_v are the bulk viscosity of the vapor and liquid phases, respectively; $\vec{F}_l$ and $\vec{F}_v$ are body forces; $\vec{F}_{lift,l}$ and $\vec{F}_{lift,v}$ are lift forces; $\vec{F}_{wl,l}$ and $\vec{F}_{wl,v}$ are wall lubrication forces; $\vec{F}_{vm,l}$ and $\vec{F}_{vm,v}$ are virtual mass forces; $\vec{F}_{td,l}$ and $\vec{F}_{td,v}$ are turbulent dispersion forces; $\vec{R}_{lv}$ and $\vec{R}_{vl}$ are interphase forces between liquid and vapor phase; K_{lv} is the interphase exchange coefficient.

To balance computational efficiency with predictive capability, only the interphase drag force and gravity are retained in the present CFD model, whereas the lift, wall lubrication, virtual mass, and turbulent dispersion forces are neglected. This simplification is physically reasonable because the primary objective of the CFD simulation is to capture the pressure distribution and gross phase-splitting behavior in the inlet header, where the flow redistribution is dominated by the pressure gradient and inertial effects. The omitted forces mainly affect the local trajectory of dispersed droplets near the walls [41] and have a minor impact on the time-averaged mass flow division among the parallel channels. Moreover, the resulting discrepancies in the local phase distribution are systematically offset by the subsequent correction using the distributed-parameter model (Section 3.5). Specifically, the empirical closure relations employed in that model are derived from experiments performed on actual corrugated PHE geometries. Hence, their friction and loss coefficients inherently account for the macroscopic effects of these unresolved inter-phase interactions.

3.2.2. Interphase Exchange Coefficient

The symmetric drag model is employed to compute the interface exchange coefficient [42] for the two-phase flow of R32, given by:

$$K_{lv} = \frac{(\alpha_l \rho_l + \alpha_v \rho_v) f}{6\tau_{lv}} d_l A_i \tag{10}$$

$$\tau_{\mathrm{lv}} = \frac{\left(\alpha_{\mathrm{l}}\rho_{\mathrm{l}} + \alpha_{\mathrm{v}}\rho_{\mathrm{v}}\right)\left[\frac{1}{2}\left(d_{\mathrm{l}} + d_{\mathrm{v}}\right)\right]^2}{18\left(\alpha_{\mathrm{l}}\mu_{\mathrm{l}} + \alpha_{\mathrm{v}}\mu_{\mathrm{v}}\right)} \tag{11}$$

$$f = \frac{C_{\mathrm{D}}Re}{24} \tag{12}$$

$$C_{\mathrm{D}} = \begin{cases} 24\left(1 + 0.15Re^{0.687}\right)/Re, & Re \le 1000 \\ 0.44, & Re > 1000 \end{cases} \tag{13}$$

$$Re = \frac{\left(\alpha_{\mathrm{l}}\rho_{\mathrm{l}} + \alpha_{\mathrm{v}}\rho_{\mathrm{v}}\right)\left|v_{\mathrm{l}} - v_{\mathrm{v}}\right|\left[\frac{1}{2}\left(\left|d_{\mathrm{l}} + d_{\mathrm{v}}\right|\right)\right]}{\alpha_{\mathrm{l}}\mu_{\mathrm{l}} + \alpha_{\mathrm{v}}\mu_{\mathrm{v}}} \tag{14}$$

where f represents the drag function, A_i is the interfacial area density. The ia-symmetric model is selected for calculation, as shown below:

$$A_{\mathrm{i}} = \frac{6\alpha_{\mathrm{v}}\alpha_{\mathrm{l}}}{d_{\mathrm{lv}}} \tag{15}$$

$$d_{\mathrm{lv}} = \begin{cases} d_{\mathrm{l}}, & \text{If the liquid phase is a dispersed phase} \\ \alpha_{\mathrm{v}}d_{\mathrm{l}} + \alpha_{\mathrm{l}}d_{\mathrm{v}}, & \text{If the liquid and vapor phase are dispersed phase} \end{cases} \tag{16}$$

3.2.3. Turbulence Model

A realizable k-ε mixture turbulence model is adopted. For two-phase flow, the turbulent kinetic energy equation and the turbulent dissipation rate equation are as follows:

$$\frac{\partial}{\partial t}\left(\rho_{\mathrm{m}}k\right) + \nabla\cdot\left(\rho_{\mathrm{m}}\vec{v}_{\mathrm{m}}k\right) = \nabla\cdot\left[\left(\mu_{\mathrm{m}} + \frac{\mu_{\mathrm{m}}}{\sigma_{\mathrm{k}}}\right)\nabla k\right] + G_{\mathrm{km}} - \rho_{\mathrm{m}}\varepsilon + G_{\mathrm{b}} - Y_M \tag{17}$$

$$\begin{aligned} &\frac{\partial}{\partial t}\left(\rho_{\mathrm{m}}\varepsilon\right) + \nabla\cdot\left(\rho_{\mathrm{m}}\vec{v}_{\mathrm{m}}\varepsilon\right) \\ = \ &\nabla\cdot\left[\left(\mu_{\mathrm{m}} + \frac{\mu_{\mathrm{m}}}{\sigma_{\varepsilon}}\right)\nabla\varepsilon\right] + \rho_{\mathrm{m}}C_1S_{\mathrm{m}}\varepsilon - \rho_{\mathrm{m}}C_2\frac{\varepsilon^2}{k + \sqrt{\nu_{\mathrm{m}}\varepsilon}} + C_{1\varepsilon}\frac{\varepsilon}{k}C_{3\varepsilon}G_{\mathrm{b}} \end{aligned} \tag{18}$$

$$\rho_{\mathrm{m}} = \alpha_{\mathrm{l}}\rho_{\mathrm{l}} + \alpha_{\mathrm{v}}\rho_{\mathrm{v}} \tag{19}$$

$$\vec{v}_{\mathrm{m}} = \frac{\alpha_{\mathrm{l}}\rho_{\mathrm{l}}\vec{v}_{\mathrm{l}} + \alpha_{\mathrm{v}}\rho_{\mathrm{v}}\vec{v}_{\mathrm{v}}}{\alpha_{\mathrm{l}}\rho_{\mathrm{l}} + \alpha_{\mathrm{v}}\rho_{\mathrm{v}}} \tag{20}$$

$$\mu_{\mathrm{m}} = \alpha_{\mathrm{l}}\mu_{\mathrm{l}} + \alpha_{\mathrm{v}}\mu_{\mathrm{v}} \tag{21}$$

$$\nu_{\mathrm{m}} = \frac{\mu_{\mathrm{m}}}{\rho_{\mathrm{m}}} \tag{22}$$

$$\mu_{\mathrm{tm}} = \rho_{\mathrm{m}}C_{\mu}\frac{k^2}{\varepsilon} \tag{23}$$

$$G_{\mathrm{km}} = \mu_{\mathrm{tm}}\left[\nabla\vec{v}_{\mathrm{m}} + \left(\nabla\vec{v}_{\mathrm{m}}\right)^{\mathrm{T}}\right]:\nabla\vec{v}_{\mathrm{m}} \tag{24}$$

3.3. Boundary Conditions

The evaporator inlet temperature is set to 15 °C, and the thermophysical properties of R32 are assumed constant and obtained from REFPROP. At this temperature, the vapor density is 35.19 kg/m^3, the vapor dynamic viscosity is 1.2258 × 10^{-5} Pa·s, the liquid density is 1000.9 kg/m^3, the liquid dynamic viscosity is 1.2731 × 10^{-4} Pa·s, and the surface tension is 8.417 × 10^{-3} N/m.

A mass flow inlet boundary condition is applied with a turbulence intensity of 5%, a hydraulic diameter of 12.7 mm, and the mass flow rate and inlet volume fraction are spec-

ified according to the respective operating conditions. The dispersed phase (liquid) droplet diameter is set to 0.02 mm. A pressure outlet boundary condition is imposed at the exit of all 26 branch channels with a gauge pressure of 0 Pa.

The solution scheme is configured with the Coupled algorithm combined with the Pseudo-Transient method to achieve steady-state convergence. For spatial discretization, the gravity term is discretized using the Least Squares Cell-Based method, the pressure term employs the PRESTO! scheme, while the momentum, turbulent kinetic energy, and turbulent dissipation rate terms are all discretized using the second-order upwind scheme. The volume fraction term is solved using the modified HRIC scheme to improve phase interface resolution and enhance numerical stability.

3.4. Mesh Generation and Independence Analysis

The poly-hexcore meshing method in ANSYS Fluent Meshing 2019 R3 is employed to generate mesh. To resolve fine-scale flow structures, local mesh refinement is applied in the inlet header region, as shown in Figure 6b.

For the operating condition with a total mass flow rate of 200 kg/h and an inlet vapor quality of 0.15, six different mesh configurations are generated. The variations in the liquid-phase mass flow rate and the standard deviation of the flow distribution σ_l across the branch channels are analyzed for each mesh, where σ_l is computed according to Equation (25).

$$\sigma_l = \sqrt{\frac{\sum_{i=1}^{N}\left(\frac{m_{l,i}}{m_{l,ave}} - 1.0\right)^2}{N}} \tag{25}$$

Here, N is the number of channels, $m_{l,i}$ is the liquid phase flow rate of the i-th channel, and $m_{l,ave}$ is the average liquid phase flow rate of all channels.

Figure 7 illustrates the liquid-phase flow rate distributions across the six mesh configurations. As the mesh density increases, the flow distribution curves converge toward a stable solution. Beyond 3.41 million cells, further refinement results in insignificant variations, thereby confirming grid independence. These qualitative observations are corroborated by the quantitative data presented in Table 4. As the mesh increases, the relative deviation of m_l decreases, and the standard deviation of the dimensionless flow distribution σ_l stabilizes, indicating good mesh convergence. When the mesh is refined from 3.41 M to 4.53 M cells, the maximum relative deviation of m_l is 8.06%, while average relative deviation of m_l decreases to 2.95%, and the relative deviation of σ_l is only 1.21%, indicating that further refinement yields negligible improvement in solution accuracy. Considering both computational accuracy and efficiency, the 3.41 M mesh is selected as the baseline for subsequent simulations.

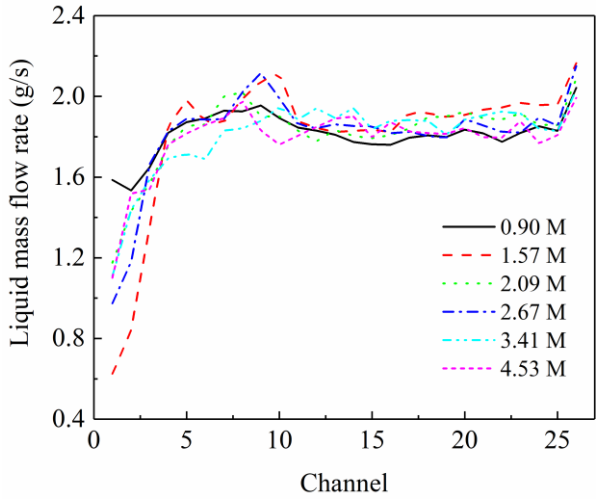

Figure 7. Liquid phase flow distribution with different mesh.

Table 4. Summary of calculation results with different mesh.

Number of Mesh	Maximum Relative Deviation of m_l	Average Relative Deviation of m_l	σ_l	Relative Deviation of σ_l
0.90 M	/	/	0.0575	/
1.57 M	60.55%	9.11%	0.1891	228.67%
2.09 M	87.23%	9.86%	0.0988	47.75%
2.67 M	17.25%	4.36%	0.1299	31.50%
3.41 M	22.29%	5.55%	0.1025	21.11%
4.53 M	8.06%	2.95%	0.1013	1.21%

3.5. Correction Method of Distributed Parameter Model

Although the simplification of the CFD model significantly reduces computational cost, it inherently introduces modeling inaccuracies. Moreover, the omission of heat transfer and the idealization of channel geometry lead to inaccurate predictions of both pressure drop and heat transfer rate, thereby compromising the fidelity of flow distribution results. To compensate for these errors, the CFD model is coupled with a distributed parameter model. The two-phase flow distribution and inlet header pressure drop obtained from CFD are used as initial inputs to the distributed parameter model, enabling an iterative solution for the overall thermal-hydraulic performance of the PHE. Based on the mass, momentum, energy conservation, and the constraint of equal pressure drop in parallel channels, the flow distribution in each channel is iteratively adjusted, thus correcting the errors introduced by model simplification.

The overall solution workflow of the flow prediction approach is schematically shown in Figure 8. First, a three-dimensional CFD model of the PHE is constructed, and the initial two-phase flow distribution is simulated using the Navier–Stokes equations and the Eulerian multiphase model. The vapor and liquid flow distributions in each channel, along with the pressure drop distributions in the inlet header from the CFD simulation, are used as initial inputs to the distributed parameter model. The flow distribution is adjusted to satisfy mass conservation, ensuring that the total system flow remains constant throughout the iteration. Subsequently, local pressure drops and heat transfer rates in the plate channels are computed using empirical correlations calibrated from experimental data or widely accepted in the literature. Based on the physical constraint of equal pressure drop in parallel channels, the vapor phase flow distribution is iteratively adjusted until the maximum pressure drop deviation across all channels falls below a prescribed convergence criterion. At convergence, the two-phase flow distribution output by the distributed parameter model is taken as the final prediction under the operating condition.

In contrast to the traditional distributed parameter model, the proposed method incorporates pressure drops predicted by CFD into Equation (1), substituting the empirical correlations previously used to estimate, thus removing reliance on empirical correlations for pressure drops in the inlet header. As a result, the method enables application to the optimization of various flow distribution structures, extending its applicability to a broader range of engineering design scenarios.

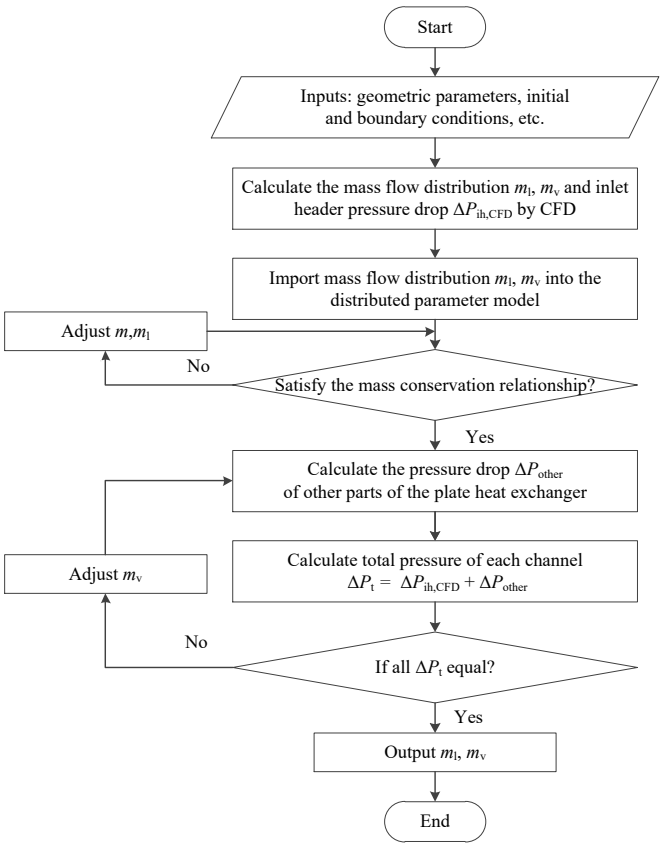

Figure 8. Iteration algorithm of the flow distribution prediction.

4. Results and Discussion

4.1. Experimental and Model Prediction Results

To validate the proposed CFD–distributed parameter model coupling method, a total of 12 test cases are designed by combining three refrigerant mass flow rates (100, 150, and 200 kg/h) with four inlet vapor qualities (0.10, 0.15, 0.20, and 0.25). The refrigerant inlet saturation temperature is maintained at 15 °C, and the water inlet temperature is fixed at 25 °C. For each test case, the water mass flow rate is adjusted to achieve an outlet superheated temperature of 9~10 °C.

The CFD simulations are performed under the same inlet conditions as the experiments. The mass flow inlet boundary is specified with a turbulence intensity of 5% and a hydraulic diameter of 12.7 mm. The dispersed liquid phase droplet diameter is set to 0.02 mm. A pressure outlet boundary with 0 Pa gauge pressure is imposed at the exits of all 26 branch channels. The thermophysical properties of R32 are evaluated at 15 °C using REFPROP.

All test conditions are summarized in Table 5.

Table 5. Test conditions of 12 cases.

Case	$m_{r,in}$ kg/h	$T_{r,in}$ °C	$x_{r,in}$ /	$T_{w,in}$ °C	$m_{w,in}$ kg/s
1	100	15	0.10	25	0.92
2	100	15	0.15	25	0.78
3	100	15	0.20	25	0.70
4	100	15	0.25	25	0.76
5	150	15	0.10	25	1.43
6	150	15	0.15	25	1.38

7	150	15	0.20	25	1.37
8	150	15	0.25	25	1.39
9	200	15	0.10	25	1.97
10	200	15	0.15	25	1.98
11	200	15	0.20	25	2.02
12	200	15	0.25	25	1.97

Figure 9 shows the IR images of the sidewalls on the water side and refrigerant side for all 12 test conditions. The phase transition boundaries identified by the algorithm [20] are overlaid as black solid lines. For each condition, the fronts on the two sides are averaged to obtain a representative phase boundary. Using this averaged boundary together with the iterative algorithm (shown in Figure 4), the experimental flow distribution in each channel is determined. The overall pressure drop and heat transfer rate are directly calculated from the measured refrigerant inlet/outlet temperature and pressure.

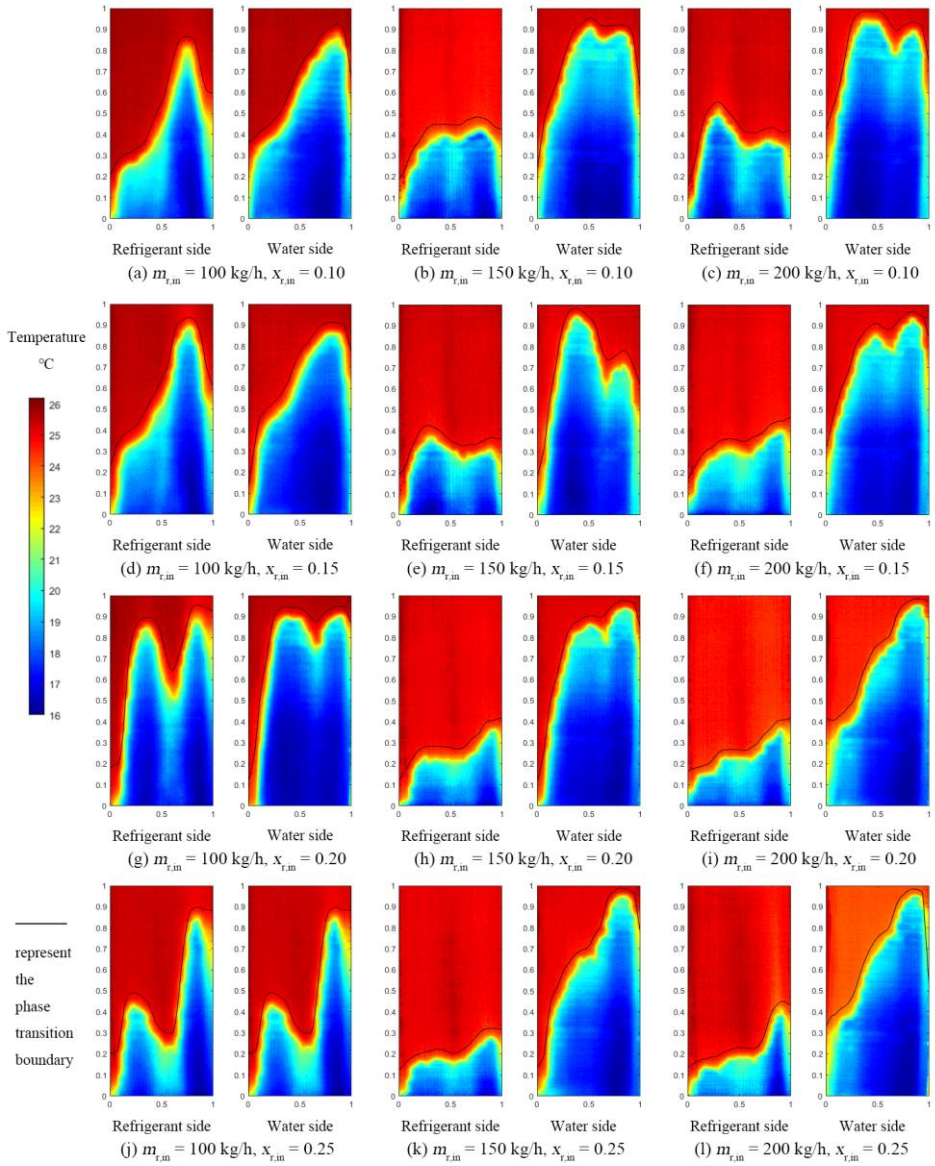

Figure 9. IR images of the sidewalls on the water side and refrigerant side.

The flow distribution and thermal performance are also predicted using the hybrid modeling approach developed in this study. The reliability of the proposed method is assessed by quantifying the discrepancies between model predictions and experimental

measurements. As shown in Figures 10 and 11, for the 12 test cases, the relative error in predicted pressure drop remains within ±10%, while that in heat transfer rate is within ±5%, indicating high predictive accuracy of the model.

Figure 12 illustrates the velocity distribution contours of the liquid phase under different operating conditions. For ease of comparison, only the central plane of the inlet header is displayed. As shown in the figure, the flow upon entering the inlet header exhibits typical high-speed jet behavior, with peak velocity at the jet center and a monotonic decrease toward the periphery. Meanwhile, the high-speed jet induces an entrainment effect, leading to the development of a local recirculation zone outside the jet region. Unlike a free jet, the pressure difference between the inlet header and the plate channels induces a bulk flow toward the channels, resulting in an overall upward motion that shifts the high-velocity core upward in the contour.

Figure 12 reveals distinct velocity distribution patterns across the tested operating conditions. At constant inlet vapor quality, as the total mass flow rate increases, the mass flow rate of the liquid refrigerant increases accordingly. However, the vapor–liquid ratio remains unchanged, resulting in a constant liquid flow area at the inlet. Consequently, the average velocity in the liquid refrigerant jet region increases. At constant total flow rate, as the inlet vapor quality increases, the liquid mass flow rate decreases and the vapor mass flow rate increases, resulting in a higher local void fraction at the inlet. It reduces the effective flow area for the liquid phase, further increasing its average velocity.

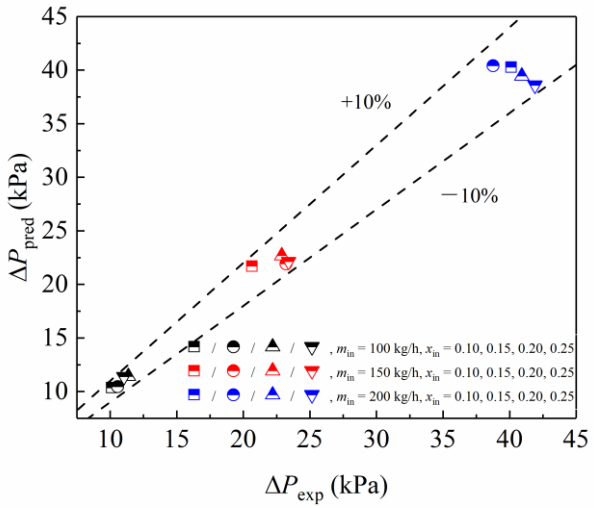

Figure 10. Comparison of pressure drop of refrigerant.

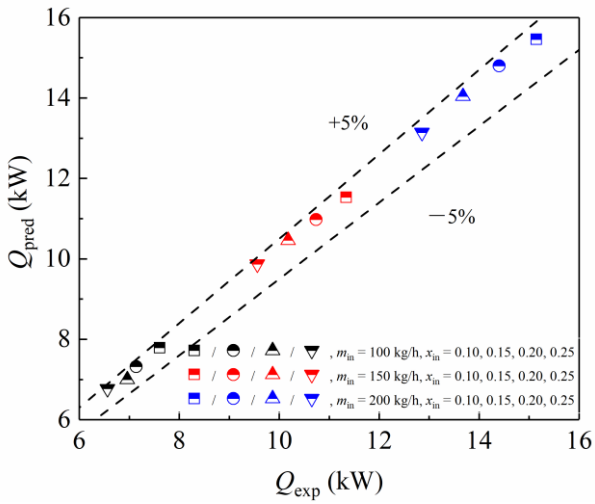

Figure 11. Comparison of heat transfer rate of refrigerant.

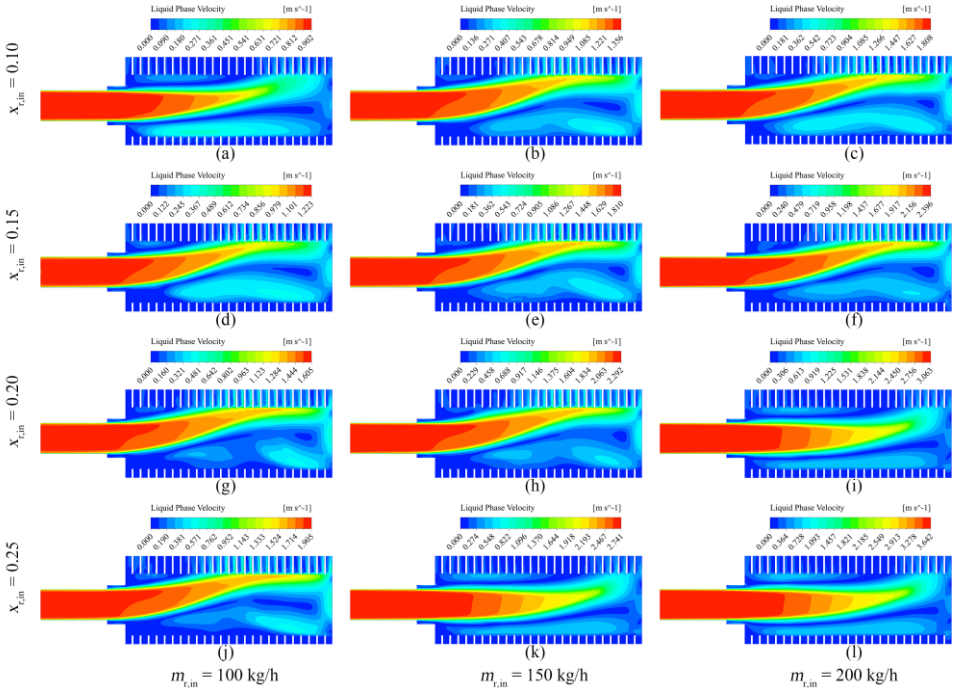

Figure 12. Contours of liquid refrigerant velocities: (**a**) $m_{r,in}$ = 100 kg/h, $x_{r,in}$ = 0.10; (**b**) $m_{r,in}$ = 150 kg/h, $x_{r,in}$ = 0.10; (**c**) $m_{r,in}$ = 200 kg/h, $x_{r,in}$ = 0.10; (**d**) $m_{r,in}$ = 100 kg/h, $x_{r,in}$ = 0.15; (**e**) $m_{r,in}$ = 150 kg/h, $x_{r,in}$ = 0.15; (**f**) $m_{r,in}$ = 200 kg/h, $x_{r,in}$ = 0.15; (**g**) $m_{r,in}$ = 100 kg/h, $x_{r,in}$ = 0.20; (**h**) $m_{r,in}$ = 150 kg/h, $x_{r,in}$ = 0.20; (**i**) $m_{r,in}$ = 200 kg/h, $x_{r,in}$ = 0.20; (**j**) $m_{r,in}$ = 100 kg/h, $x_{r,in}$ = 0.25; (**k**) $m_{r,in}$ = 150 kg/h, $x_{r,in}$ = 0.25; (**l**) $m_{r,in}$ = 200 kg/h, $x_{r,in}$ = 0.25.

Figure 13 illustrates the predicted two-phase flow distribution under various operating conditions. The proposed method predicts physically plausible flow distribution curves across all conditions, with overall trends in close agreement with experimental measurements. Across all test cases, the mean absolute relative error for the liquid flow rate is below 12%, for the vapor below 48%, and for the total flow rate below 3%, demonstrating the model's accuracy in predicting total and liquid distribution despite higher uncertainty in vapor flow partitioning.

It can be noted that the relatively large vapor-phase error occurs predominantly in channels where the experimental vapor flow rate is near zero. In these channels, the absolute deviations are small, but the relative error is inflated by the small denominator. Since the vapor-phase refrigerant in these channels has a small impact on the heat transfer and pressure drop of the heat exchanger, this error has little effect on the overall predictions (Figures 8 and 9). Therefore, the vapor-phase error does not compromise the model's utility for engineering design.

The flow distribution patterns in Figure 13 correlate well with the velocity structures observed in Figure 12, indicating a strong link between jet dynamics and flow distribution. For cases with significant upward deflection of the high-velocity jet, the liquid is preferentially directed into the channels near the inlet, resulting in a bimodal distribution (peaking near the inlet, decreasing mid-way, and rising again at the downstream end). In contrast, when the jet deflection is minimal, the liquid phase is predominantly distributed into the downstream channels, with the flow rate increasing progressively along the flow direction.

Further analysis reveals that the proposed method achieves high prediction accuracy under low vapor quality conditions ($x_{in} \leq 0.20$), with simulated flow distributions in close

agreement with experimental results. However, prediction accuracy degrades at higher vapor qualities, particularly when the liquid-phase flow distribution exhibits a bimodal pattern, as the model struggles to resolve such complex non-uniform structures.

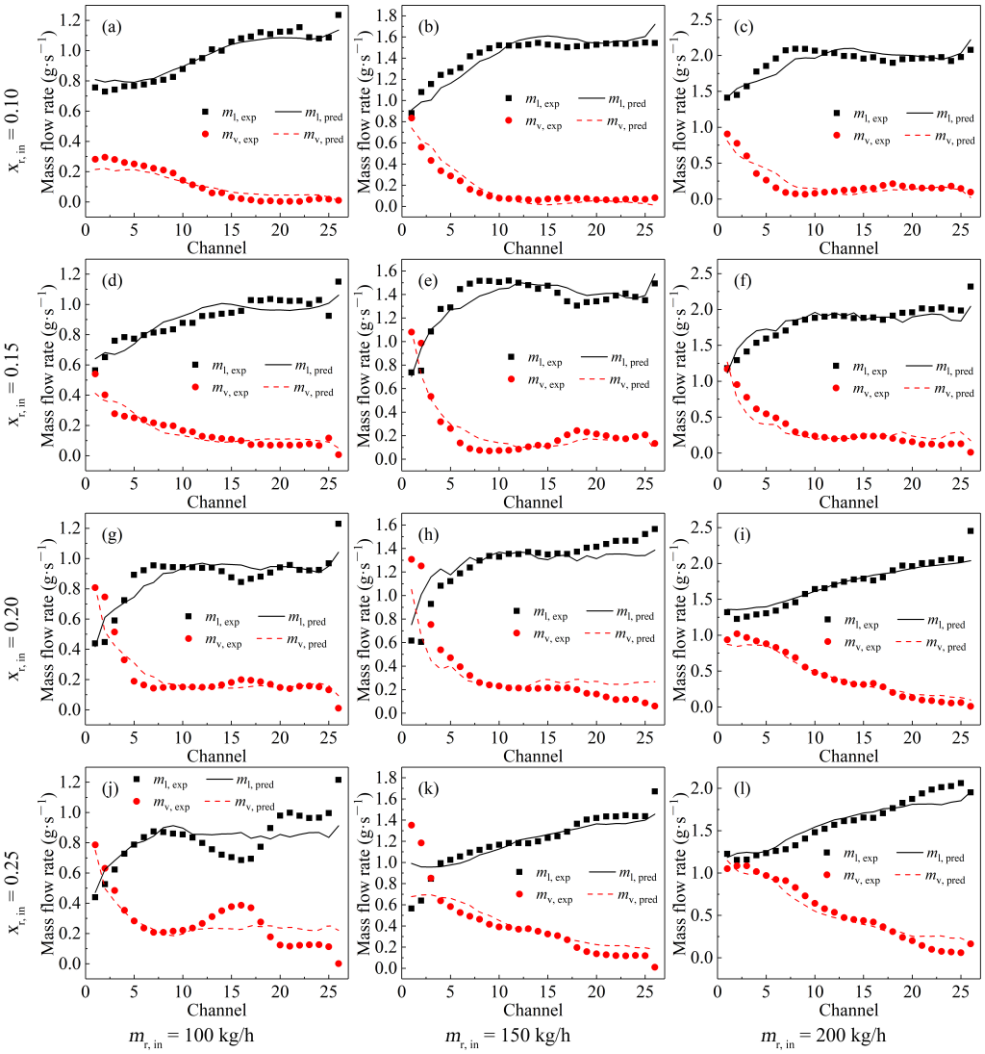

Figure 13. Two-phase refrigerant flow distribution: (**a**) $m_{r,in}$ = 100 kg/h, $x_{r,in}$ = 0.10; (**b**) $m_{r,in}$ = 150 kg/h, $x_{r,in}$ = 0.10; (**c**) $m_{r,in}$ = 200 kg/h, $x_{r,in}$ = 0.10; (**d**) $m_{r,in}$ = 100 kg/h, $x_{r,in}$ = 0.15; (**e**) $m_{r,in}$ = 150 kg/h, $x_{r,in}$ = 0.15; (**f**) $m_{r,in}$ = 200 kg/h, $x_{r,in}$ = 0.15; (**g**) $m_{r,in}$ = 100 kg/h, $x_{r,in}$ = 0.20; (**h**) $m_{r,in}$ = 150 kg/h, $x_{r,in}$ = 0.20; (**i**) $m_{r,in}$ = 200 kg/h, $x_{r,in}$ = 0.20; (**j**) $m_{r,in}$ = 100 kg/h, $x_{r,in}$ = 0.25; (**k**) $m_{r,in}$ = 150 kg/h, $x_{r,in}$ = 0.25; (**l**) $m_{r,in}$ = 200 kg/h, $x_{r,in}$ = 0.25.

The model's limited capability to predict bimodal flow structures arises from three primary factors. First, as discussed in Section 3.2, the channel geometry is simplified to a rectangular cross-section and the turbulence-enhancing effect of plate corrugations is neglected to maintain computational feasibility for the full-scale header simulation. This simplification may introduce discrepancies in the predicted local pressure distribution within the header, particularly under complex flow conditions. Second, the accuracy of two-phase CFD simulations depends on multiple factors, such as turbulence modeling, interface exchange force closures, and mesh resolution. Under the present modeling framework, the droplet diameter is assumed constant and interphase forces (lift, wall lubrication, and turbulent dispersion) are neglected. While these simplifications are acceptable for the macroscopic distribution in the header region, they may contribute to the observed discrepancies at high vapor qualities ($x \geq 0.25$), where complex phase interactions become more pronounced. Third, although the mesh has been locally refined in the inlet

header region, the poly-hexcore mesh employed in this study is generated via an automated procedure that does not incorporate regional partitioning or boundary-conforming cell treatments. The absence of tailored mesh topology may contribute to the deteriorated predictive performance under bimodal flow conditions. Therefore, future work will address these limitations by incorporating a population balance model for droplet size evolution and by evaluating cut-cell or regionally partitioned mesh strategies [43,44] to further enhance predictive fidelity across a broader range of conditions.

4.2. Influence of Outlet Conditions on PHE Performance

The indirect flow measurement method relies on the phase transition boundary identified from an infrared camera. Therefore, under conditions with low or zero outlet superheated temperature, distinct superheated regions may not develop in certain channels, hindering accurate identification of the phase boundary and thereby limiting the method's applicability. In contrast, the proposed flow prediction method effectively overcomes these limitations and is independent of outlet conditions.

This study focuses on a 54-plate chevron-type plate heat exchanger to systematically investigate the influence of outlet conditions on thermal-hydraulic performance. To ensure comparability, the refrigerant mass flow rate is set to 200 kg/h, the inlet vapor quality to 0.15, the refrigerant inlet temperature to 15 °C, and the water inlet temperature to 25 °C. The outlet superheated temperature is controlled by adjusting the water flow rate, and the operating conditions are summarized in Table 6.

Table 6. Effect of different operating conditions on flow distribution.

$m_{r,in}$ kg/h	$T_{r,in}$ °C	$x_{r,in}$ /	$T_{w,in}$ °C	$m_{w,in}$ kg/s	State /	T_{sh} °C	x_{out} /
200	15	0.15	25	0.55	Superheat	10.40	1.00
200	15	0.15	25	0.49	Superheat	9.79	1.00
200	15	0.15	25	0.44	Superheat	7.55	1.00
200	15	0.15	25	0.41	Superheat	4.00	1.00
200	15	0.15	25	0.38	Two-phase	0.00	0.99
200	15	0.15	25	0.36	Two-phase	0.00	0.95
200	15	0.15	25	0.33	Two-phase	0.00	0.91
200	15	0.15	25	0.27	Two-phase	0.00	0.80

Figure 14 illustrates the variations in pressure drop and heat transfer rate across different outlet conditions. Analysis of Table 6 and Figure 14 reveals that, as the water temperature remains higher than that of the refrigerant, the heat transfer rate increases with the water mass flow rate, leading to a gradual rise in outlet vapor quality. When the water flow rate exceeds 0.38 kg/s, the refrigerant exits in the superheated regime. With further increases in water flow rate, the outlet superheated temperature increases monotonically.

The pressure drop across the PHE depends strongly on the refrigerant outlet state. When the outlet refrigerant is two-phase, the pressure drop increases with increasing water flow rate due to rising outlet vapor quality. In contrast, when the outlet is superheated, the pressure drop decreases with increasing water flow rate as the superheated temperature increases. This behavior stems from the inherent differences in flow resistance between single-phase and two-phase refrigerant flow.

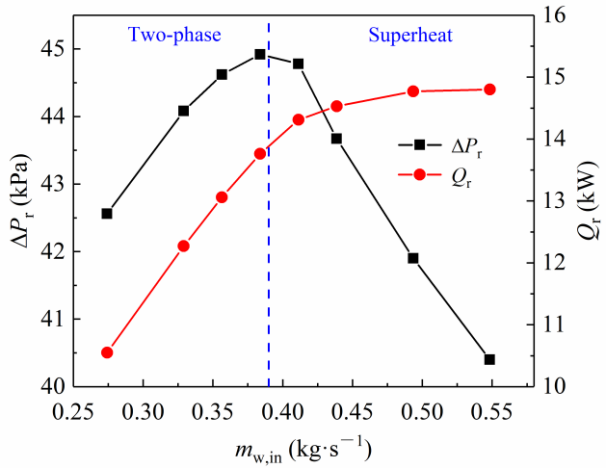

Figure 14. The pressure drop and heat transfer rate under different outlet conditions.

For identical channel geometry and mass flow rate, the pressure drop of two-phase flow exceeds that of superheated vapor. When the refrigerant outlet is superheated, the outlet superheated temperature increases as the water flow rate increases. This increase in superheated temperature leads to the expansion of the superheated region and the contraction of the two-phase region, thereby reducing the overall two-phase flow resistance. Consequently, the overall pressure drop decreases (see Figure 15).

For the same increment in water flow rate, the variation in two-phase region length within the channels is markedly different depending on the outlet state. When the outlet is superheated, the average normalized two-phase region length decreases from 0.79 to 0.57 as the water flow rate increases by 0.11 kg/s, a reduction of 27.85%. In contrast, when the outlet is two-phase, the length decreases from 0.98 to 0.93 for the same increment, a reduction of only 5.10%. Therefore, the influence of water flow rate on the two-phase region fraction is significantly greater when the outlet is superheated than when it is in the two-phase state.

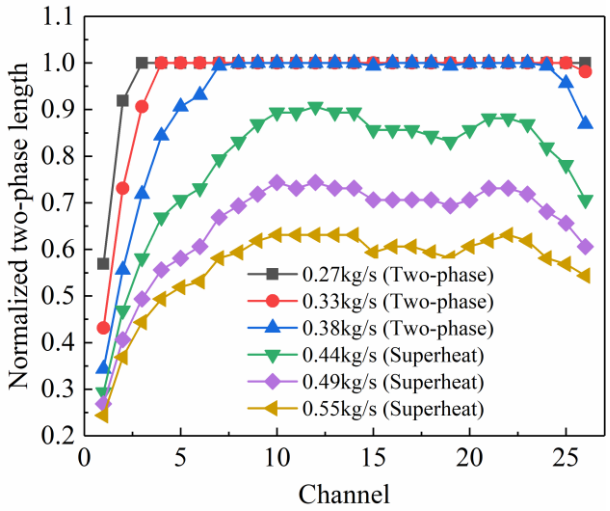

Figure 15. Normalized two-phase length under different outlet conditions.

At constant refrigerant mass flow rate and flow area, the vapor phase velocity exceeds the liquid phase velocity because of its significantly lower density. As shown in Figure 16, when the refrigerant outlet is two-phase and the inlet vapor quality is fixed, increasing the water flow rate results in higher outlet and average vapor quality, as well

as an increased vapor phase fraction. The increased vapor phase fraction raises the average flow velocity, enhancing two-phase frictional losses and leading to a rise in pressure drop with increasing water flow rate, which is driven by the increase in outlet vapor quality. When the refrigerant outlet is two-phase, increasing the water flow rate by 0.11 kg/s raises the outlet quality from 0.80 to 0.99, and the average vapor quality across channels increases from 0.4793 to 0.5684, representing an 18.59% increase. In contrast, under superheated outlet conditions, the outlet vapor quality is fixed at 1.00, and the average vapor quality increases only marginally with water flow rate: a 0.11 kg/s increase raises it from 0.5757 to 0.5762, corresponding to a 0.09% change. Therefore, the water flow rate has a markedly stronger influence on mean vapor quality when the outlet is two-phase than when it is superheated.

In summary, when the outlet is two-phase, the pressure drop is primarily governed by the outlet vapor quality and increases with superheated temperature. In contrast, when the outlet is superheated, the pressure drop is dominated by the two-phase region fraction and decreases with increasing superheated temperature.

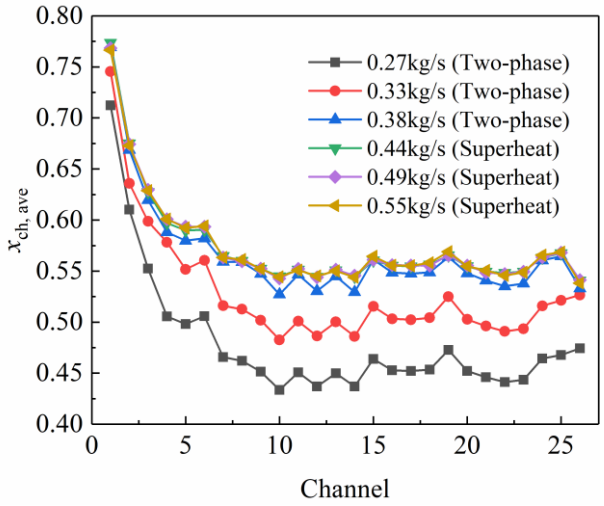

Figure 16. Average vapor quality under different outlet conditions.

Similar to the pressure drop, the heat transfer rate also depends on the refrigerant outlet condition. As shown in Figure 14, for both outlet states, the heat transfer rate increases monotonically with increasing water flow rate, but the rate of increase differs markedly. The rate of heat transfer increase is higher under two-phase outlet conditions than under superheated conditions. This phenomenon is mainly related to the large deviation of the convective heat transfer coefficient of the refrigerant in two-phase and superheated states, as well as the large difference in heat transfer temperature difference between the water and refrigerant.

As shown in Figure 17, at the same mass flow rate, the convective heat transfer coefficient of two-phase refrigerant substantially exceeds that of superheated vapor. When the refrigerant outlet is superheated, although the water-side heat transfer rate increases with flow rate, the rising outlet superheated temperature expands the superheated region at the expense of the two-phase region. The refrigerant temperature approaches the water temperature, thereby reducing the logarithmic mean temperature difference ΔT_m. When the water flow rate increases by 0.11 kg/s, the average logarithmic mean temperature difference decreases from 2.50 °C to 1.66 °C, representing a reduction of 33.6% and contributing to a modest increase in overall heat transfer rate.

Under two-phase outlet conditions, the two-phase region occupies a larger fraction of the channels, thereby dominating the heat transfer process. The increases with water

flow rate: a 0.11 kg/s increment raises it from 3.50 °C to 3.70 °C, representing an increase of 5.71%.

The increased water flow rate not only enhances the $\Delta T_{m,ave}$ but also raises the water-side convective heat transfer coefficient due to higher velocity. As the water flow rate increases, the refrigerant outlet vapor quality rises, and the refrigerant convective heat transfer coefficient rises concurrently. Consequently, the overall heat transfer coefficient increases, leading to a significant rise in heat transfer rate. Therefore, the rate of heat transfer increase under two-phase outlet conditions exceeds that under superheated conditions.

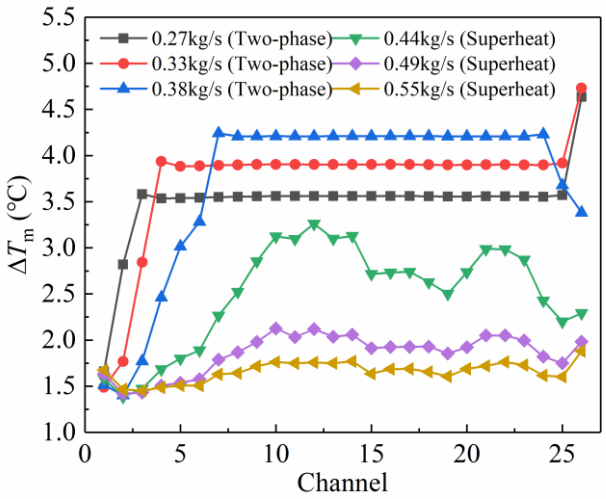

Figure 17. Logarithmic mean temperature difference under different outlet conditions.

4.3. Flow Distribution and Performance of a Distributor-Equipped PHE

To verify the feasibility of the proposed method for flow distributor structural optimization, a geometrically simplified annular distributor with a single orifice [45] is selected as a case study, as shown in Figure 18. This distributor is located at the interface between the refrigerant inlet header and the plate channels of the PHE. The annular structure blocks the direct flow path, thereby preventing the refrigerant from entering the plate channels directly. Instead, the refrigerant is forced to mix within the inlet header before exiting through a small orifice in the annular structure. With this configuration, the pressure distribution among the channels is significantly altered. When properly designed, the flow distribution uniformity is greatly improved, leading to enhanced heat transfer performance of the PHE.

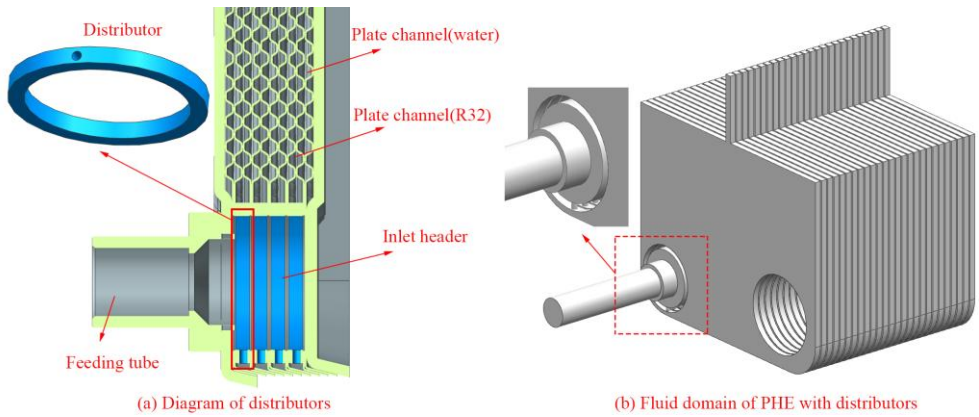

Figure 18. Distributor-equipped PHE and fluid domain.

In practical refrigeration system operation, the outlet temperature must be maintained within a stable range to ensure both system efficiency and safety. The system operates under the following conditions: a refrigerant mass flow rate of 200 kg/h, an inlet vapor quality of 0.15, a water flow rate of 0.40 kg/s, a refrigerant inlet temperature of 15 °C, and a water inlet temperature of 25 °C. For the PHE without a distributor, the outlet superheated temperature is 2.23 °C. This value lies within the normal operating range of 2~3 °C, which is necessary for stable system performance. When the original PHE is replaced with a distributor-equipped PHE, the improved flow distribution alters the outlet superheated temperature. To maintain the superheated temperature within the original normal range, the system must be controlled by adjusting the refrigerant flow rate or optimizing the water-side operating parameters. However, since water temperature and flow rate are typically dictated by user demand and exhibit limited adjustability, the conventional control strategy focuses on regulating the refrigerant mass flow rate.

Under the same operating conditions, the orifice diameter of the distributor is fixed at 2 mm, and the orifice orientation is sequentially set to 0°, 45°, 90°, 135°, 180°, 225°, 270°, and 315°. The calculated results are summarized in Table 7. As shown in the table, when the outlet superheat is maintained within the 2~3 °C range, the σ_1 is significantly reduced after installing the distributors, with a minimum value of 0.0330. The corresponding heat transfer rate increases by up to 4.33%.

Table 7. Performance under different orifice orientations.

Degree °	$m_{r,in}$ kg/h	$T_{r,in}$ °C	$x_{r,in}$ /	$m_{w,in}$ kg/s	$T_{w,in}$ °C	T_{sh} °C	ΔP_r kPa	Q_r kW	σ_1 /
None	200.0	15	0.15	0.40	25	2.23	44.91	14.11	0.1025
0	206.0	15	0.15	0.40	25	2.15	51.12	14.54	0.0774
45	207.0	15	0.15	0.40	25	2.18	51.40	14.54	0.0876
90	207.0	15	0.15	0.40	25	2.33	52.01	14.64	0.0621
135	207.0	15	0.15	0.40	25	2.25	52.10	14.64	0.0474
180	207.5	15	0.15	0.40	25	2.22	52.34	14.65	0.0541
225	208.0	15	0.15	0.40	25	2.25	52.98	14.72	0.0330
270	206.0	15	0.15	0.40	25	2.32	51.35	14.58	0.0705
315	208.0	15	0.15	0.40	25	2.22	52.33	14.63	0.0775

Figure 19 presents the predicted flow distribution results for different distributor configurations. As previously analyzed, the liquid phase tends to migrate toward regions far from the inlet, while the vapor phase accumulates near the inlet. With the installation of a flow distributor, the refrigerant can no longer exit freely through the corner ports and must instead enter the plate channels via orifices on the distributor.

When the orifices are oriented downward (0°, 45°, and 315°), gravity drives a portion of the liquid phase to preferentially pass through the orifices into the front channels, resulting in a high liquid fraction and low vapor fraction in the upstream channels. As the flow progresses, the two-phase mixture gradually re-entrains, and the vapor phase is carried downstream by the liquid into the mid-channel regions. The remaining liquid phase concentrates toward the far-inlet region due to inertia, while the low-inertia vapor phase occupies a smaller proportion in these regions. Consequently, the liquid-phase mass flow rate exhibits a trend of first decreasing and then increasing, while the vapor-phase flow rate follows the opposite variation.

When the orifices are oriented upward (135°, 180°, and 225°), the vapor phase first contacts the orifices and exits through the near-inlet channels. However, due to its lower density, the vapor mass flow rate through the orifices is relatively low, leading to a more uniform flow distribution across channels compared to the downward-facing case. Much

of the vapor phase fails to enter the front channels promptly and instead mixes with the liquid phase, weakening the initial phase separation effect. This promotes the uniform dispersion of the liquid phase under vapor entrainment, resulting in a flatter flow distribution. As a result, the σ_1 is smaller, indicating improved flow uniformity.

When the orifices are oriented at the intermediate angles (90° and 270°), the flow distribution lies between the two extreme cases. The liquid-phase mass flow rate follows a multi-peak variation, first decreasing, then increasing, followed by a second decrease and a final increase. The troughs in the liquid-phase distribution curve and the corresponding peaks in the vapor-phase curve are relatively shallow and smooth, indicating weak phase separation and more thorough mixing.

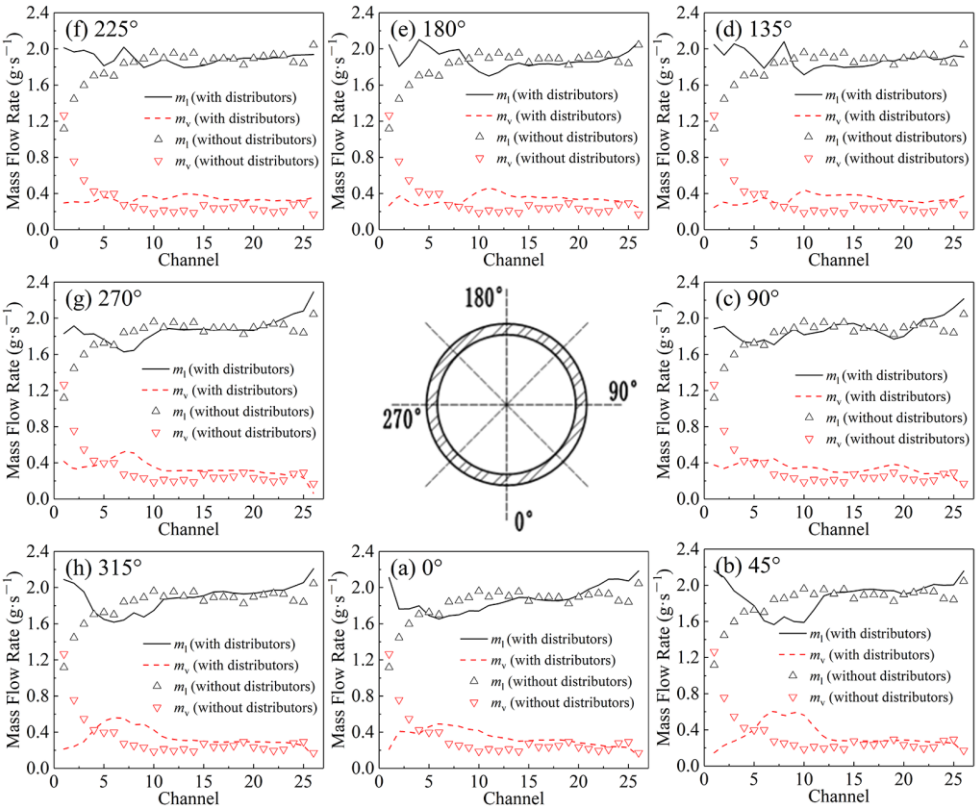

Figure 19. Flow distribution for different orifice orientations (orifice diameter is 2.0 mm): (**a**) 0°; (**b**) 45°; (**c**) 90°; (**d**) 135°; (**e**) 180°; (**f**) 225°; (**g**) 270°; (**h**) 315° (orifice orientation).

Based on the analysis of Table 7 and Figure 19, the optimal orifice orientation of the distributor can be determined to maximize heat transfer performance. Using the same analytical approach, the influence of other geometric parameters, such as orifice diameter, orifice depth, and distributor ring diameter, on flow distribution uniformity, pressure drop, and thermal performance can be systematically evaluated, enabling a comprehensive structural optimization of the flow distributor.

In summary, the proposed method is effective for multi-parameter optimization of distributor design, offering significant engineering value in improving design efficiency.

5. Conclusions

This study proposes a two-phase flow prediction method that couples CFD simulations with a corrected distributed parameter model. The proposed method couples a geometrically simplified CFD simulation with a distributed parameter model for channel-level correction, thereby making full-scale PHE simulations computationally feasible without resolving the costly corrugated details. An experimental platform for indirect

flow measurement was established and tests were conducted on a 54-plate PHE under 12 distinct operating conditions to validate the proposed model. Comparisons between experimental results and model predictions demonstrate high accuracy across all test conditions. The average relative error in liquid-phase flow rate per channel is below 12%, while the average error in total mass flow rate is less than 3%. The prediction errors for pressure drop and heat transfer rate remain within ±10% and ±5%, respectively. These results confirm the model's high accuracy and robust performance across a wide range of operating conditions. By adjusting the water flow rate, we systematically investigated the influence of the refrigerant outlet state on overall performance. The results confirm the method's applicability under varying outlet conditions. Furthermore, the mechanism by which orifice orientation in the flow distributor influences flow distribution uniformity and thermal performance is revealed. For the tested annular distributor, the optimal orifice orientation is identified as 225°, which reduces the liquid maldistribution standard deviation by 67.8% and increases the overall heat transfer rate by 4.33% compared with the distributor-free design. This finding highlights its critical role in enhancing heat exchanger performance and demonstrates the method's engineering potential for optimizing distributor structures.

In summary, the proposed method offers three key advantages: (i) eliminating the reliance on empirical correlations for inlet header pressure drop, thereby enabling flexible adaptation to various distributor designs; (ii) significantly reducing computational cost compared to full-scale CFD while maintaining engineering accuracy; and (iii) applicability under low or zero superheat conditions, where indirect methods fail. However, the model has limitations. It treats plate channels as smooth ducts, neglecting corrugation-induced turbulence and header heat transfer. Additionally, assuming constant droplet diameter and ignoring lift, wall lubrication, and turbulent dispersion forces may reduce accuracy at high vapor qualities (≥0.25). Since validation is limited to one PHE geometry and specific conditions, extrapolation to other plate patterns or refrigerants requires further work. Future research will extend this method to diverse geometries and working fluids, refine the CFD model with variable droplet sizes and interfacial forces, and couple it with multi-objective optimization for automated distributor design.

Author Contributions: Conceptualization, L.H.; methodology, Z.Y.; software, Q.L.; validation, B.L.; formal analysis, S.Z.; resources, Z.L. All authors have read and agreed to the published version of the manuscript.

Funding: This research was funded by the Basic and Applied Basic Research Foundation of Zhuhai, China, grant number 2220004003028 and the National Key Research and Development Program of China, grant number 2022YFB4003801.

Data Availability Statement: Data will be made available on request.

Acknowledgments: We thank to anonymous reviewers for their useful comments and suggestions which helped improve the presentation of the manuscript.

Conflicts of Interest: The authors declare no conflicts of interest.

Abbreviations

Nomenclature

A	area, m^2
A_i	interfacial area density, kg/m^3
d	diameter, m
f	drag function, N
F	force, N

g	gravitational acceleration, m/s^2
K	interphase exchange coefficient
k	turbulent kinetic energy, m^2/s^2
L_{tp}	two-phase length, m
m	mass flow rate, kg/h
m	mass transfer, kg/s
N	number of channels
P	pressure, kPa
Q	heat transfer rate, W
R	interphase force, N
Re	Reynolds number
U	overall heat transfer coefficients, W/(m^2·K)
v	velocity, m/s
x	vapor quality
ΔP	pressure drop, kPa
ΔT_m	logarithmic mean temperature difference, ℃
ε	turbulent dissipation rate, m^2/s^2
Greek symbols	
α	volume fraction
μ	dynamic viscosity coefficient, Pa·s
ρ	density, kg/m^3
σ	standard deviation
τ	stress-strain tensor, N/m^2
subscripts	
ave	average
eff	effective
exp	experimental data
ih	inlet header
l	liquid phase
left	the left boundary of element
lv	from liquid phase to vapor phase
m	mixture
oh	outlet header
pred	predicted value
r	refrigerant
right	the right boundary of element
sh	superheat
tp	two-phase
turn-in	turning-in
turn-out	turning-out
v	vapor phase
vl	from vapor phase to liquid phase
w	water

References

1. Song, J.H.; Lei, L.; Zhou, N.X.; Zhang, J.Z. Research Progress on Heat Transfer of Herringbone Plate Heat Exchangers Under Single-Phase/Two-Phase Flow. *Energies* **2026**, *19*, 249.
2. Zhang, J.; Desideri, A.; Kærn, M.R.; Ommen, T.S.; Wronski, J.; Haglind, F. Flow boiling heat transfer and pressure drop characteristics of R134a, R1234yf and R1234ze in a plate heat exchanger for organic Rankine cycle units. *Int. J. Heat Mass Transf.* **2017**, *108*, 1787–1801.
3. Osakabe, M.; Hamada, T.; Horiki, S. Water flow distribution in horizontal header contaminated with bubbles. *Int. J. Multiph. Flow* **1999**, *25*, 827–840.
4. Fei, P.; Hrnjak, P.S. Adiabatic Developing Two-Phase Refrigerant Flow in Headers of Heat Exchangers. Doctor's Thesis, University of Illinois Urbana-Champaign, Champaign, IL, USA, 2004.
5. Lee, J.K.; Lee, S.Y. Distribution of two-phase annular flow at header–channel junctions. *Exp. Therm. Fluid Sci.* **2004**, *28*, 217–222. https://doi.org/10.1016/S0894-1777(03)00042-6.

6. Marchitto, A.; Devia, F.; Fossa, M.; Guglielmini, G.; Schenone, C. Experiments on two-phase flow distribution inside parallel channels of compact heat exchangers. *Int. J. Multiph. Flow* **2008**, *34*, 128–144.
7. Kim, N.; Han, S. Distribution of air-water annular flow in a header of a parallel flow heat exchanger. *Int. J. Heat Mass Transf.* **2008**, *51*, 977–992.
8. Dario, E.R.; Tadrist, L.; Oliveirac, J.L.G.; Passos, J.C. Measuring maldistribution of two-phase flows in multi-parallel microchannels. *Appl. Therm. Eng.* **2015**, *91*, 924–937.
9. Wijayanta, A.T.; Miyazaki, T.; Koyama, S. Refrigerant distribution in horizontal headers with downward minichannel-branching conduits: Experiment, empirical correlation and two-phase flow pattern map. *Exp. Therm. Fluid Sci.* **2017**, *81*, 430–444.
10. Vist, S.; Pettersen, J. Two-phase flow distribution in compact heat exchanger headers. *Exp. Therm. Fluid Sci.* **2004**, *28*, 209–215.
11. Ahmad, M.; Berthoud, G.; Mercier, P. General characteristics of two-phase flow distribution in a compact heat exchanger. *Int. J. Heat Mass Transf.* **2009**, *52*, 442–450.
12. Kim, N.; Byun, H. Effect of inlet configuration on upward branching of two-phase refrigerant in a parallel flow heat exchanger. *Int. J. Refrig.* **2013**, *36*, 1062–1077.
13. Zou, Y.; Hrnjak, P. Effects of fluid properties on two-phase flow and refrigerant distribution in the vertical header of a reversible microchannel heat exchanger-Comparing R245fa, R134a, R410A, and R32. *Appl. Therm. Eng.* **2014**, *70*, 966–976.
14. Mahvi, A.J.; Garimella, S. Two-phase flow distribution of saturated refrigerants in microchannel heat exchanger headers. *Int. J. Refrig.* **2019**, *104*, 84–94.
15. Li, H.; Hrnjak, P. Quantification of liquid refrigerant distribution in parallel flow microchannel heat exchanger using infrared thermography. *Appl. Therm. Eng.* **2015**, *78*, 410–418.
16. Li, J.; Hrnjak, P. An experimentally validated model for microchannel condensers with separation circuitry. *Appl. Therm. Eng.* **2021**, *183*, 114–116.
17. Navarro, E.; Alvarez-Piñeiro, L.; Albaladejo, P.; Schnabel, L. Refrigerant maldistribution in brazed plate heat exchanger evaporators. Part A: Testing campaign and experimental results. *Int. J. Refrig.* **2021**, *131*, 119–128.
18. Navarro, E.; Alvarez-Piñeiro, L.; Schnabel, L.; Corberan, J.M. Refrigerant maldistribution in brazed plate heat exchanger evaporators. Part B: Analysis of the influence of maldistribution on the evaporator performance. *Int. J. Refrig.* **2021**, *131*, 312–321.
19. Li, W.Z.; Hrnjak, P. Visualization of two-phase refrigerant flow in the inlet header of brazed plate heat exchangers and its effect on distribution. *Int. J. Refrig.* **2021**, *131*, 483–492.
20. Li, W.Z.; Hrnjak, P. Quantification of two-phase refrigerant distribution in brazed plate heat exchangers using infrared thermography. *Int. J. Refrig.* **2021**, *131*, 348–358.
21. Zhang, S.; Li, Y.; Xu, Y.; Yang, J.; Wang, Q. A new method for estimating the refrigerant distribution in plate evaporator based on infrared thermal imaging. *Int. J. Refri.* **2021**, *126*, 57–65.
22. Li, Y. Study on Fluid Distribution in Plate Evaporator Based on Infrared Thermal Imaging. Doctor's Thesis, Zhejiang University, Hangzhou, China, 2020.
23. Buell, J.R.; Soliman, H.M.; Sims, G.E. Two-phase pressure drop and phase distribution at a horizontal tee junction. *Int. J. Multiph. Flow* **1994**, *20*, 819–836.
24. Joyce, G.; Soliman, H.M. Pressure drop for two-phase mixtures combining in a tee junction with wavy flow in the combined side. *Exp. Therm. Fluid Sci.* **2016**, *70*, 307–315.
25. Lu, P.; Deng, S.; Zhao, L.; Shao, Y.; Zhao, D.; Xu, W.; Zhang, Y.; Wang, Z. Analysis of pressure drop in T-junction and its effect on thermodynamic cycle efficiency. *Appl. Energy* **2018**, *231*, 468–480.
26. Li, W.Z. Flow Distribution in Brazed Plate Heat Exchangers. Doctor's Thesis, University of Illinois Urbana-Champaign, Champaign, IL, USA, 2021.
27. Zahrani, S.A.; Islam, M.S.; Saha, S.C. Heat transfer enhancement of modified flat plate heat exchanger. *Appl. Therm. Eng.* **2021**, *186*, 116533.
28. Jafari, A.; Sadeghianjahromi, A.; Wang, C. Experimental and numerical investigation of brazed plate heat exchangers—A new approach. *Appl. Therm. Eng.* **2022**, *200*, 117694.
29. Galeazzo, F.C.C.; Miura, R.Y.; Gut, J.A.W.; Tadini, C.C. Experimental and numerical heat transfer in a plate heat exchanger, Chem. *Eng. Sci.* **2006**, *61*, 7133–7138.
30. Pawar, N.; Maurya, R.S. Flow maldistribution in a simplified plate heat exchanger model—A numerical study. *Appl. Mech. Mater.* **2012**, *110*, 2529–2536.
31. Qiu, J.; Wei, W.; Zhang, S.; Chen, G. Research on performance of distributors used in plate heat exchangers based on cfd numerical simulation. *J. Mech. Eng.* **2010**, *46*, 130–137.

32. Zhang, Y.; Han, W.; Shuai, W.; Song, X.; Shi, J.; Chen, J. Experimental and simulation study on the distributor design in plate evaporators. *Int. J. Refrig.* **2022**, *143*, 126–137.
33. Mudhafar, M.A.H. Numerical study of two-phase flow in multi-channels plate heat exchanger. *Int. Commun. Heat Mass Transf.* **2022**, *138*, 106380.
34. Ham, J.; Lee, G.; Kwon, O.; Bae, K.; Cho, H. Numerical study on the flow maldistribution characteristics of a plate heat exchanger. *Appl. Therm. Eng.* **2023**, *224*, 120136.
35. Li, W.Z.; Hrnjak, P. Single-phase flow distribution in brazed plate heat exchangers: Experiments and models. *Int. J. Refrig.* **2021**, *126*, 45–56.
36. Li, W.Z.; Hrnjak, P. Compensating for the end plate effect on heat transfer in brazed plate heat exchangers. *Int. J. Refrig.* **2021**, *126*, 99–108.
37. Almalfi, R.L.; Vakili, F.F.; Thome, J.R. Flow boiling and frictional pressure gradients in plate heat exchangers: Part 2. Comparison of literature methods to database and new prediction methods. *Int. J. Refrig.* **2015**, *61*, 185–203.
38. Collier, J.G.; Thome, J.R. *Convective Boiling and Condensation*, 3rd ed.; McGraw-Hill: Oxford, UK, 1994.
39. Panda, K.; Hirokawa, T.; Huang, L. Design study of microchannel heat exchanger headers using experimentally validated multiphase flow CFD simulation. *Appl. Therm. Eng.* **2020**, *178*, 115585.
40. Pao, W.; Saieed, A.; Hashim, F.M.; Norpiah, R.B.M. Numerical simulation of two-phase separation in a small diameter ratio T-junction. *Mater. Werkst.* **2017**, *48*, 255–260.
41. Wang, X.; Guo, X.; Li, Z.; Wang, H. Numerical study of void fraction distribution in horizontal bubbly flow using a Euler–Euler two-fluid model. *Appl. Sci.* **2026**, *16*, 3841.
42. ANSYS Fluent Theory Guide—14.5.7. Interphase Exchange Coefficients. Available online: https://ansyshelp.ansys.com/public/account/secured?returnurl=/Views/Secured/corp/v261/en/flu_th/flu_th_sec_eulermp_theory_exchange.html%23flu_th_multi_symdrag (accessed on 19 May 2026).
43. Abumandour, R.M.; El-Reafay, A.M.; Salem, K.M.; Dawood, A.S. Numerical Investigation by Cut-Cell Approach for Turbulent Flow through an Expanded Wall Channel. *Axioms* **2023**, *12*, 442.
44. Salem, K.M.; Elrefaay, A.M.; Abumandour, R.M.; Dawood, A.S. Modeling two-phase gas-solid flow in axisymmetric diffusers using cut cell technique: An Eulerian-Eulerian approach. *Bound. Value Probl.* **2024**, *2024*, 150.
45. Kim, B.; Jeon, Y.; Lee, D. Heat transfer and hydrodynamic characteristics of R-1336mzz(Z) as an alternative to R-245fa in a brazed plate heat exchanger with a distributor. *Int. Commun. Heat Mass Transf.* **2025**, *166*, 109170.